



## Evaluation of 940 nm Diode Laser in Esthetic Crown Lengthening

Noor Ali Dween<sup>1\*</sup>, Mohammed K. Dhahir<sup>1</sup>, Tahrir N. Aldelaimi<sup>2</sup>

*\*Corresponding Authors: [nour.ali1202a@ilps.uobaghdad.edu.iq](mailto:nour.ali1202a@ilps.uobaghdad.edu.iq)  
[mohammed@ilps.uobaghdad.edu.iq](mailto:mohammed@ilps.uobaghdad.edu.iq)  
[tahrir.aldelaimi@uoanbar.edu.iq](mailto:tahrir.aldelaimi@uoanbar.edu.iq)*

1. Laser Institute for Postgraduate Studies, University of Baghdad, Baghdad, Iraq
2. College of Dentistry, University of Anbar, Iraq

(Received 23/07/2022; accepted 20/02/2023)

**Abstract Background:** Crown lengthening is a surgical procedure that apically positions the gingival edge and/or removes supporting bone in order to increase the amount of supra gingival tooth structure for restorative or cosmetic purposes.

**The objective of the study:** The purpose of this study was to evaluate the efficacy of the 940nm diode laser in esthetic crown lengthening surgery through clinical observations, patient questionnaires, clinical photographs, and gingival healing following gingival operations. **Material and methods:** In this randomized clinical trial, 16 patients (11 females and 5 males) had their crowns surgically lengthened using a diode laser (940 nm) in continuous wave (CW) mode with 1 watt energy settings. A visual analogue scale is used on the first, third, seventh, and twenty-first days following surgery to record pain, swelling, bleeding, functional interference, tooth sensitivity, and success from an aesthetic standpoint, as well as overall patient satisfaction based on patient opinion and clinical photographs. **Results:** In the present study, we noticed that the scale of pain, bleeding, oedema, function interference, and tooth sensitization significantly decreased gradually during the first two visits. The measured parameters completely disappeared after one week in most cases, as well as increase patient satisfaction and aesthetic achievement. The patients were recalled three weeks later, the wounds had totally healed, and the patient were not complaining of any pain. **Conclusion:** Crown lengthening requires optimal gingival margin design. This involves precise shaping of delicate tissues, which is difficult with the scalpel. While Lasers give improved gingival sculpting control and can be used for aesthetic crown lengthening. The laser surgery has many advantages, including excellent hemostasis with little or no bleeding, being less invasive and sterile wound cut, causing less pain and suffering during and after surgery, and enhancing patient satisfaction since the operation is short and, in most circumstances, relatively painless. Also, in laser surgery, there is less functional interruption and enhanced patient satisfaction since a periodontal pack is not needed to cover the surgery site. The healing is faster and more aesthetic when using laser surgery procedure.

**Keywords:** diode laser, esthetic, crown lengthening, scalpel surgery, laser surgery, visual analogue scale (vas)

## Introduction

A pleasing smile is seen as a symbol of attractiveness in modern society (Cairo et al., 2012). A beautiful smile is influenced by the hard tissue components (such as teeth), the degree of gingival appearance, and the lip shape (Manjula et al., 2015). Gingival health is one of the primary fundamental aesthetic goals to take into account when formulating a treatment plan. Additionally important are the gingiva's margin and shape. The remaining ridges of the maxilla and mandible in the oral cavity are covered by the keratinized epithelium known as gingiva, which also extends to the mucogingival junction in the vestibule (Wahyuni et al., 2021).

Crown lengthening is a surgical procedure that lengthens the supragingival tooth structure. A gingivectomy, also referred to as crown lengthening, is a surgical procedure that involves removing and reforming the gingival margin in order to achieve aesthetic, functional, or restorative objectives (Nield-Gehrig and Willmann, 2007). Several surgical techniques that all attempt to improve the appearance of the gingiva and teeth may be used to extend crowns. When reshaping the marginal gingiva, care must be taken to preserve the biologic width. Sometimes osseous recontouring is needed to keep the biologic width and place the margins correctly (Shivaprasad et al., 2015).

Crown lengthening surgery was esthetic or functional, depending on the patient. "Esthetic crown lengthening" refers to increasing the length of the tooth structure for aesthetic purposes, such as in the case of patients with short clinical crowns and gummy smiles related to altered passive eruption; while "restorative/functional crown lengthening" refers to exposing a fractured tooth or sub gingival caries (Hempton and Dominici, 2010). Crown lengthening procedures that are both practical and aesthetically are recommended in several clinical situations (Farista et al.,

2016). Crown lengthening is utilized for excessive gingival exposure, a "gummy smile," from inadequate passive eruption, or "short teeth." Short clinical crowns are teeth with fewer than 2 mm of sound, opposing parallel walls following occlusal and axial reduction (Rabie et al., 2013). Crown lengthening may be performed using a scalpel, electrosurgery, or a laser.

Compared to other technologies, lasers provide various advantages. Laser therapy is effective and produces good outcomes and patient satisfaction. The mechanism of the laser's action on tissue is determined by the laser settings and the properties of the tissue. Different types of lasers are used in periodontal surgery, including Nd:YAG, diode, CO<sub>2</sub>, and the Erbium laser family (Musaa et al., 2017). Due to the many benefits of lasers, they rapidly gained a significant role in dentistry, especially soft tissue lasers for oral surgery, which are progressively preferred over traditional techniques due to their good hemostasis, accessibility of the wound area, reduced edema, very limited area of thermal necrosis in surrounding tissues, reduced post-operative pain, and potential to perform operations without anesthesia (Al-Jumaily, 2019). The diode laser is one of the most commonly used laser systems. It is mostly utilized in soft tissue applications. In this randomized clinical trial, using a diode laser (940 nm) in continuous wave (CW) mode with 1 watt energy settings for aesthetic crown lengthening.

## Material and methods

Sixteen people between the ages of 15 and 42 participated in this study. They were either healthy or had a well-controlled systemic illness. The periodontal area must be in excellent health. This may be assessed by evaluating the gingival bleeding score, gingival inflammatory score, and gingival pocket probing depth. Also, another inclusion criteria involved patients who had gingival exposure between 4 and 6 mm due to a short clinical crown or an imbalance of

tooth length and gingival margins. as well as patients who require crown lengthening therapy due to gingival enlargement caused by prostheses, orthodontics, or after healing of periodontal disease, or plaque that induced gingival enlargement. Demographic information such as the patient's age and gender, medical and dental histories, clinical examination, and the number of teeth involved in the operation, which must be at least four, were collected. Aesthetic crown lengthening by gingivectomy was performed at the University of Baghdad, Faculty of Dentistry, Department of Periodontology, by using a 940 nm diode laser. All treatments were carried out after the patient was informed about the goal of this study and gave informed consent. All participants were given oral hygiene guidelines as well as phase I periodontal therapy at the beginning of the study. The patients' gingival contours were assessed after one week for aesthetic crown lengthening operations. Before scaling, the plaque index (pl), bleeding on probing, and gingival index (GI) were all calculated. Chu aesthetic gauges were used on patients who had gingival exposure when smiling as a result of incorrect passive eruption and a short clinical crown. Gauges were used as recommendations to identify the right occlusogingival clinical dimension of the tooth in proportion to its width and the correct papilla position in relation to its length. Postoperative pain, edema, bleeding, functional interference, tooth sensitivity, healing, aesthetic achievement, and patient satisfaction were assessed at 1, 3, 7, and 21 days. Postoperative parameters were measured using the visual analogue scale (VAS). The VAS scale is used to assess subjective feelings like pain and other discomforts. In the present study, researchers used a traditional VAS in which a dentist wrote a vertical sign ranging from 0 (no symptoms) to 3 (severe symptoms) (the highest degree of symptoms) at each postoperative appointment.

## **Procedure**

Following the use of a periodontal probe to identify the cemento-enamel junction (CEJ), the surgical region was anesthetized with enough infiltration. The alveolar bone height and the position of supra-crestal soft tissues are both determined by the bone-sounding procedure. By placing a periodontal probe or Chu's bone sounding gauges into the sulcus, mark the bleeding areas using a pocket depth indicator. After initializing the fiber tip in contact mode, use sweeping brushing strokes and beveled incisions. The power was selected after the desired effect (excision of diseased tissue without tissue harm) was achieved using 1 W of 940 nm diode laser in continuous wave mode with a fiber-optic delivery system (fiber tip 400  $\mu$ m). An assistant was instructed to maintain irrigation with normal saline to cool the tissue and clean the surgical site, as well as to keep the vacuum tips close to the operational site to suck up any smoke or odor that could result from laser tissue ablation. Wet gauze was used to clean the surgical site and tip. The laser was interrupted every 15 seconds to evaluate gingival tissue and minimize overheating. Aesthetic crown lengthening by laser technique with follow up assessment shown in figure (1).

## **Statistical analysis:**

The data was entered into the SPSS V26 statistical program, and descriptive statistics were displayed in tables and graphs.

While the Friedman test was utilized to assess progress in the study's dependent parameters, P value 0.05 was regarded as the cutoff point of significance.



**Fig. 1:** (A) A preoperative perspective (B) intra-operative perspective, (C) immediate post-operative perspective, and (D) 3 days postoperatively (E) one week postoperative surgery (F) three-weeks post-operative perspective, (G) after bleaching and direct filing treatment.

### Results

This study included 16 participants (11 females and 5 men) who underwent surgical esthetic crown lengthening by diode laser (940nm). They ranged in age from 15 to 42 years old, with 37.8% being teenagers and 62.5% being adults. As shown table (1)

**Table 1:** distribution of studied cases based on the age and the gender of the participations

		N	%
Age	<20 year	6	37.5%
	=>20 year	10	62.5%
Gender	Male	5	31.3%
	Female	11	68.8%

The levels of pain, bleeding, swelling, functional interference (FI), and tooth sensitivity (TS) were significantly decreased throughout the time of measurement. according to the Fridman test, p value 0.05 for all circumstances, as shown in Table 2. Healing, aesthetic accomplishment (AA), and satisfaction levels were found to be consistent and to have grown considerably throughout research phases. P= 0.001 in all circumstances.

**Table 2:** The Friedman test demonstrates how pain, edema, bleeding, patient satisfaction, and function vary during an assessment

Variable	Time	Mean±std	Median (IQR)	Ranks	P value
Pain	1 <sup>st</sup> day	1.06±0.68	1(.75)	2.78	0.001
	3 <sup>rd</sup> day	0.13±0.34	.00	1.69	
	7 <sup>th</sup> day	0.00	.00	1.53	
Bleeding	1 <sup>st</sup> day	0.38(0.5)	1(1)	2.31	0.009
	3 <sup>rd</sup> day	0.13(0.342)	1	1.94	
	7 <sup>th</sup> day	0.00	0	1.75	
Edema	1 <sup>st</sup> day	0.19	0	1.56	0.157
	3 <sup>rd</sup> day	0.06	0	1.44	
FI	1 <sup>st</sup> day	0.69±0.479	1(1)	3.47	0.001
	3 <sup>rd</sup> day	0.13±342	0	2.34	
	7 <sup>th</sup> day	.00	0	2.09	
Healing	1 <sup>st</sup> day	.63±0.5	1(1)	1.44	0.001
	3 <sup>rd</sup> day	1±0.	1(0)	1.81	
	7 <sup>th</sup> day	1.88±0.5	2(0)	2.91	
	21 <sup>st</sup> day	2.81±0.75	3(0)	3.84	
TS	1 <sup>st</sup> day	0.38±0.619	0(1)	1.66	0.025
	3 <sup>rd</sup> day	0	0	1.34	
AA	1 <sup>st</sup> day	1.88±0.342	2(0)	1.41	0.001
	3 <sup>rd</sup> day	2.19±0.544	2(0)	1.97	
	7 <sup>th</sup> day	2.88±0.342	3(0)	3.31	
Satisfaction	1 <sup>st</sup> day	2±0	2(0)	1.25	0.001
	3 <sup>rd</sup> day	2.63±0.5	3(1)	2.50	
	7 <sup>th</sup> day	2.94±0.25	3(0)	3.13	
	21 <sup>st</sup> day	2.94±0.25	3(0)	3.13	

**Table3:** shows the patient distribution based on the scores of measured variables (pain, bleeding, edema, functional interference and healing) at the time of each patient's measurements. (R1= 1day, R2=3 days, R3=7 days, R4=21days)

	Pain				Bleeding				oedema				FI				Healing			
	R 1	R 2	R 3	R 4	R 1	R 2	R 3	R 4	R 1	R 2	R 3	R 4	R 1	R 2	R 3	R 4	R 1	R 2	R 3	R 4
1	2	0	0	0	0	0	0	0	1	1	0	0	1	1	0	0	0	1	2	3
2	1	0	0	0	1	1	0	0	0	0	0	0	0	0	0	0	0	1	2	3
3	0	0	0	0	0	0	0	0	0	0	0	0	0	0	0	0	0	1	2	3
4	1	0	0	0	1	1	0	0	0	0	0	0	1	0	0	0	0	1	2	3
5	1	0	0	0	0	0	0	0	0	0	0	0	1	1	0	0	1	1	2	3
6	0	0	0	0	0	0	0	0	0	0	0	0	1	0	0	0	1	1	2	3
7	2	0	0	0	1	0	0	0	1	0	0	0	1	0	0	0	1	1	2	3
8	1	0	0	0	0	0	0	0	0	0	0	0	1	0	0	0	1	1	2	3
9	1	0	0	0	0	0	0	0	0	0	0	0	1	0	0	0	1	1	2	3
0	0	0	0	0	0	0	0	0	0	0	0	0	0	0	0	0	1	1	2	3
1	1	0	0	0	0	0	0	0	1	0	0	0	0	0	0	0	0	1	2	3
1	2	0	0	0	1	0	0	0	0	0	0	0	1	0	0	0	0	1	2	3
1	1	1	0	0	0	0	0	0	0	0	0	0	0	0	0	0	1	1	2	3
1	2	1	0	0	0	0	0	0	0	0	0	0	1	0	0	0	1	1	2	3
1	1	0	0	0	1	0	0	0	0	0	0	0	1	0	0	0	1	1	2	3
1	1	0	0	0	1	0	0	0	0	0	0	0	1	0	0	0	1	1	2	3

**Table 4:** The distribution of studied patients based on measured variable scores (teeth sensitivity TS, aesthetic achievement AA and patient satisfaction) at the time of each patient's measurements.

(R1= 1day, R2=3 days, R3=7 days, R4=21days)

	TS				AA				Satisfaction			
	R1	R2	R3	R4	R1	R2	R3	R4	R1	R2	R3	R4
1	0	0	0	0	2	2	3	3	1	2	3	3
2	1	0	0	0	2	2	3	3	1	2	3	3
3	0	0	0	0	2	3	3	3	1	3	3	3
4	0	0	0	0	2	2	3	3	1	3	3	3
5	1	0	0	0	2	3	3	3	1	2	3	3
6	0	0	0	0	2	2	3	3	1	3	3	3
7	2	0	0	0	1	2	3	3	1	2	3	3
8	0	0	0	0	2	2	3	3	1	3	3	3
9	0	0	0	0	2	2	3	3	1	3	3	3
10	0	0	0	0	2	3	3	3	1	3	3	3
11	0	0	0	0	2	3	3	3	1	3	3	3
12	0	0	0	0	1	1	2	2	1	2	3	3
13	0	0	0	0	2	2	3	3	1	2	2	3
14	1	0	0	0	2	2	3	3	1	3	3	3
15	1	0	0	0	2	2	2	2	1	3	3	3
16	0	0	0	0	2	2	3	3	1	3	3	3

**Discussion**

Esthetic crown lengthening is a secure and reliable way to maintain healthy dentogingival relationships. The laser may be utilized in place of conventional techniques for numerous intraoral soft tissue surgical operations. Crown lengthening has been performed using a variety of lasers, including Nd:YAG, Er, Cr:YSGG, Er:YAG, carbon dioxide, and diodes (Verma et al., 2012). Diode lasers may operate in continuous or pulsed mode and produce near-infrared laser light with a wavelength of 810 to 980 nanometers. These wavelengths are readily absorbed by hemoglobin and pigment, which make up the majority of soft tissue. Diode lasers may thus be used for incision, excision, coagulation, and pain treatment. This clinical study evaluated the efficiency of a 940nm diode in soft tissue crown lengthening. Postoperative pain, bleeding, oedema, functional interference, healing, tooth sensitivity, aesthetic accomplishment, and patient satisfaction were evaluated using visual analog scales. The data showed a considerable reduction in pain on the 1st and 3rd days, which disappeared on the 3rd (7 days) and 4th (21 days) visits. This is due to

the laser's influence on prostaglandin production and its sealing action on nerve terminals (Abdulkareem et al., 2021). edema and bleeding scores were significantly decreased across time of treatment in laser due to the laser's ability to control bleeding during surgery by closing small blood vessels and blocking lymph vessels helps prevent post-operative issues such as swelling and edema. Over time, the functional interference score declined significantly. Since a coagulated layer develops over the surgical incision after laser surgery, there is no need to cover the surgical site with a periodontal pack. Laser treatment enhances wound healing by accelerating epithelial cell mobility and fibroblast proliferation. Immune cells like neutrophils and macrophages release cytokines and growth hormones during this period (Subramanya, 2022). The healing score increased with time in this study. Additionally, in this trial, the tooth sensitivity score decreased significantly with time. Aesthetic achievement was evaluated in this study. Participants responded significantly to esthetic improvements after a week because lasers coagulate tissue, making it easier to visualize the operative area directly after surgery. That made the

patient more satisfied throughout the treatment. In this investigation, the aesthetic accomplishment and patient satisfaction scores increased dramatically throughout treatment.

### Conclusion

Esthetic crown lengthening is important to produce appropriate gingival margin morphology. This requires an accurate tissue incision, which is difficult with traditional (scalpel) treatments. Insufficient scalpel design for a smooth gingival margin curvature leads to uneven margins with tattered edges. The surgeon typically deviates from the original gingival margin design to minimize tissue scarring. Lasers allow more control over gingival sculpting and should be included in the aesthetic crown lengthening arsenal. Diode lasers are beneficial in respect of operator control, ease, and ablation accuracy.

### REFERENCES

- Al-Jumaily HA. *The effect of 2 different techniques in second stage implant surgery*. Journal of Baghdad College of Dentistry. 2019 Mar 15;31(1):25-30.
- Abdulkareem Hussain Alwan, et. al. "Gingivectomy by Diode Laser and Conventional Method (A Comparative Study)." IOSR Journal of Dental and Medical Sciences (IOSR-JDMS), 20(07), 2021, pp. 56-61
- Cairo F, Graziani F, Franchi L, Defraia E, Pini Prato GP. *Periodontal plastic surgery to improve aesthetics in patients with altered passive eruption/gummy smile: a case series study*. International journal of dentistry. 2012 Sep 30;2012.
- Farista S, Kalakonda B, Koppolu P, Baroudi K, Elkhatat E, Dhaifullah E. *Comparing laser and scalpel for soft tissue crown lengthening: a clinical study*. Glob J Health Sci. 2016 Oct 1;8(10):55795.
- Hempton TJ, Dominici JT. *Contemporary crown-lengthening therapy: a review*. The Journal of the American Dental Association. 2010 Jun 1;141(6):647-55.
- Manjula WS, Sukumar MR, Kishorekumar S, Gnanashanmugam K, Mahalakshmi K. *Smile: A review*. Journal of pharmacy & bioallied sciences. 2015 Apr;7(Suppl 1):S271.
- Musaa FE, Awazli LG, Alhamdani F. *Gingival enlargement management using diode laser 940 nm and conventional scalpel technique (A comparative study)*. Iraqi Journal of Laser. 2017;16(B):1-9.
- Nield-Gehrig JS, Willmann DE. *Foundations of periodontics for the dental hygienist*. Lippincott Williams & Wilkins; 2007.
- Rabie AB, To TN, Wong RW, McGrath CP. *The adjunct effectiveness of diode laser gingivectomy in maintaining periodontal health during orthodontic treatment: A randomized controlled clinical trial*. The Angle Orthodontist. 2013 Jan;83(1):43-7.
- Shivaprasad BM, Rakesh MP, Prabhu SS. *Esthetic Correction of Gummy Smile by Gingivectomy using Diode Laser*. J Health Sci Res 2015;6(1):17-21.
- Subramanya AP. *Evaluation of Healing Effect of Laser Bandage Following Gingivectomy-A Case Report*. Journal of Dental Implants and Lasers. 2022 Jan;1(1).
- Verma SK, Maheshwari S, Singh RK, Chaudhari PK. *Laser in dentistry: An innovative tool in modern dental practice*. National journal of maxillofacial surgery. 2012 Jul;3(2):124.
- Wahyuni IS, Zakiawati D, Hidayat W. *Pigmentasi Mukosa Mulut*. Penerbit NEM; 2021 Dec 7.

## تقييم الدايدود ليزر ذو الطول الموجي 940 نانومتر في إطالة التاج التجميلي

نور علي دوين<sup>1\*</sup> محمد كريم ظاهرا<sup>1</sup> تحرير نزال<sup>2</sup>

1 معهد الليزر للدراسات العليا / جامعة بغداد - العراق

2. كلية طب الاسنان/جامعة الانبار- العراق

**الخلاصة الخلفية والمعلومات :** إطالة التاج هو إجراء جراحي يتم فيه وضع حافة اللثة بشكل قمعي و/او ازالة العظام الداعمة من اجل زيادة كمية بنية الاسنان فوق اللثة للاغراض الترميمية او التجميلية.

**الهدف من الدراسة:** الهدف من هذه الدراسة هو تقييم فعالية ليزر الدايدود 940 نانومتر في جراحة اطالة التاج التجميلي من خلال الملاحظات السريرية واستبيانات المرضى والصور السريرية وشفاء اللثة بعد العملية

**المواد والطرق:** في هذه الدراسة السريرية العشوائية ,تم إطالة تيجان 16 مريضاً (11 انثى و 5 ذكور ) جراحياً باستخدام ليزر الدايدود (940 نانو متر) في وضع الموجة المستمرة مع اعدادات الطاقة 1 واط. تم استخدام المقياس التناظري البصري في اليوم الاول والثالث والسابع والحادي والعشرين بعد الجراحة لتسجيل الالم والتورم والنزيف والتداخل الوظيفي وحساسية الاسنان والنجاح من الناحية الجمالية فضلاً عن الرضى العام للمريض بناء على رأي المريض والصور الفوتوغرافية.

**النتائج:** في هذه الدراسة , لاحظنا ان حجم الالم والنزيف والوذمة والتداخل الوظيفي وحساسية الاسنان قد انخفض بشكل تدريجي خلال اول زيارتين , اختفت المعلومات التي تم قياسها تماماً بعد اسبوع واحد في معظم الحالات , كم تحسن ايضاً رضا المريض والتحصيل الجمالي . تم استدعاء المرضى بعد ثلاثة اسابيع , وقد التئمت الجروح تماماً ولم يشكو المرضى من اي نوع من الانزعاج .

**الخلاصة:** يتطلب اطالة التاج تصميماً مثالياً لهوامش اللثة. يتضمن هذا التشكيل الدقيق للانسجة الرقيقة وهو امر صعب باستخدام المشروط لكن يعطي الليزر تحكماً محسناً في نحت اللثة ويمكن استخدامه لالة التاج التجميلي. هنالك العديد من المزايا لجراحة الليزر , بما في ذلك الارقاء الممتاز مع القليل من النزيف او عدم وجود النزيف على الاطلاق ,كونه اقل تدخلاً وتعميقاً للجرح مما يسبب المأ ومعاناة اقل اثناء الجراحة وبعدها وتعزيز رضا المريض لان العملية قصيرة وغير مؤلمة في معظم الحالات .ايضاً في جراحة اللثة يكون هناك انقطاع وظيفي اقل ورضا افضل للمرضى نظراً لعدم الحاجة الى حزمة اللثة لتغطية موقع الحراحة .كذلك الشفاء اسرع واكثر جمالية عند استخدام الليزر للجراحة.



## Angular Laser Cleaning of Aluminum Al-4004 with Different Spot Sizes

Iman Shakir Tawfeeq\*, Zaid Aeyad Taha

\*Corresponding author: [iyman.shaker1201@lips.uobaghdad.edu.iq](mailto:iyman.shaker1201@lips.uobaghdad.edu.iq)

[ziad@ilps.uobaghdad.edu.iq](mailto:ziad@ilps.uobaghdad.edu.iq)

*Institute of Laser for Postgraduate Studies, University of Baghdad, Baghdad, Iraq*

(Received 02/09/2022; accepted 24/01/2023)

**Abstract:** When it comes to applications in welding, cutting, and surface engineering, the utilization of high-power fiber-delivered beams from solid-state lasers offers several benefits. This paper addresses the issue of cleaning the surface of the samples with different spot sizes (50, 100 and 200) (industrial ytterbium fiber laser) to prepared it to be welded. Angular laser cleaning with incident angles (5, 10, 15, 20, 25, 30) ° with different powers (3, 5, 7, 10) W and hatch distance 0.001 was use for implemented.

**Keyword:** angular laser cleaning, spot sizes and ytterbium fiber laser.

### 1. Introduction

Laser cleaning will have a significant impact on the future of cleaning operations. Environmentally hazardous products can now be cleaned without the need of mechanical or chemical procedures [1, 2]. Since there is now a dedicated community that utilizes lasers for this purpose and prominent restoration institutes have recognized the new technology, the success of laser cleaning for cultural heritage has been proven, which has led to an increase in the replacement of chemical treatments with these new techniques. As a result, this has led to an increase in the usage of these new techniques in place of chemical applications [3,4]. Laser cleaning is a technique that employs the use of pulsed laser light to either begin the process of removing pollution from a surface or to assist in this process [4, 5]. The fact that contamination, such as micron and submicron-sized particles, can have a significant influence on optics, semiconductor production, and data storage devices because of the way in which they can

get in the way of certain processes has been a driving force behind research in this area. Surface laser cleaning difficulties that involve soiling substances in the form of microscopic particles and films arise in a wide variety of human undertakings, including but not limited to manufacturing, building, art conservation, and medical [7]. Laser cleaning can be accomplished.

#### 1.1. Angular laser cleaning

Unlike typical laser cleaning, this method irradiates the metal surface from multiple angles. The laser beam is aimed towards the target material at an angular angle of incidence appropriate for the target material [15]. as can be observed in Figure 1. The beam is aimed at the surface at a using a variety of processes, including vaporization, spallation, evaporation pressure, photon pressure dries, steam, thermal heating, and laser shock cleaning [8, 9]. It was discovered that the cleaned area irradiated at an angular laser cleaning angles was up to 10 times bigger than the average laser-cleaned

area when utilizing a perpendicular angle, which means that it is significant to employ in angular cleaning [10 -14]. In this study, an angular laser cleaning technique is used instead of a perpendicular laser cleaning technique with varying spot sizes to remove the oxide layer from aluminum 4004 alloy, which is then ready for welding. variety of angles that are less than ninety degrees (angle  $90^\circ$ ). In comparison to traditional laser cleaning, this method offers a plethora of benefits, one of which is a significant increase in cleaning effectiveness. In addition, cleaning threshold fluences are decreased at angular laser cleaning angles, which, in comparison to perpendicular laser.

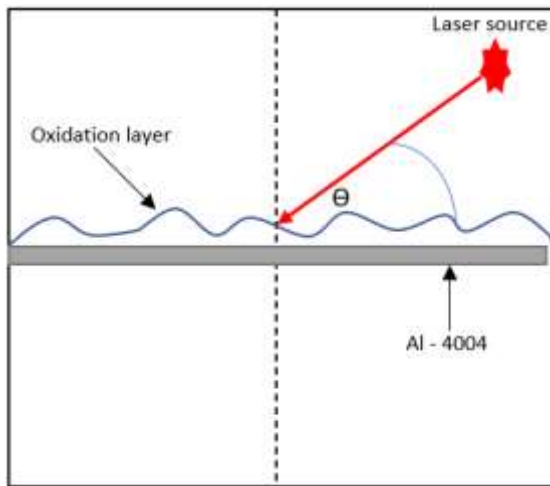


Fig. 1: angular laser cleaning

### 1.2. Aluminum alloy 4004

Since there is a lot of silicon in the 4000 series of alloys, they are not often used for extrusion applications. They are used in a lot of things, like welding wire and brazing wire, among other things. These alloys are used in sheet metal, forgings, welding, and brazing products, among other things. 4004 aluminum alloy could have a Si content of up to 11% [17]. To weld 4004 aluminum alloy, the oxide layer must be removed first [18 -21]. Because of the surrounding environment, the natural oxidation layer formed on the aluminum alloy 4004's surface. cleaning, results in a diminished danger of surface damage [16]. Figure 2. Illustrated the aluminum alloy 4004.

### 1.3. Fiber laser

An industrial ytterbium fiber laser with a wavelength of 1064nm was built at the University of Baghdad's Institute of Laser for Postgraduate Studies. The speed of the laser beam scanning was between 2 and 8000 mm/s, and the laser power ranged from 1 to 10 W at a frequency of 20 to 80 kHz. The pulse width was set at 10 s, and the spot size varied from 50 to 200 m. Figure 3 shows how the fiber laser scanned, which looked like a zig-zag.



Fig. 2: Aluminium 4004 alloy.



Fig. 3: scanning strategy of fiber laser zig-zag shaped wave..

## 2. Material and method

### 2.1 Material

The sample used was aluminum 4004 (Al 90.25% + Si 9.75%  $\pm$  0.75%), the material standard according to the international organization for standardization (IOS) equivalents of alloy, manufactured by (BAUHAUS, Sweden). Sample dimensions 2\textit{times}2 cm<sup>2</sup> and thickness of 2mm. All samples were surface cleaned with diluted ethanol before using laser cleaning.

**2.2. Experiment procedure**

With pulse repetition rate (PRR) (2, 4, 6, 8)Hz, spot size (50, 100, 200) $\mu$ m and power (3, 5, 7, 10) W and hatch 0.001 $\mu$ m with angular angles cleaning( $\theta =$ 5, 10, 15, 20, 25, 30)  $^{\circ}$ . So, remaining hatch lay outside the scope of this paper. A laser cleaning procedure has been carried out on aluminum alloy 4004 to remove a thin oxidation coating. The laser used in this work was a microsecond fiber laser (ytterbium fiber laser) with a pulse duration of 10  $\mu$ s and a fundamental wavelength of 1064 nm. The laser beam hit the target after passing through a quartz lens with a focal length of 163mm. This study's angular laser cleaning method is illustrated shown in Fig. 4. The beam focus on the surface at angles ( $\theta =$ 5, 10, 15, 20, 25, 30) $^{\circ}$ . Table 1. illustrates the parameters used at the angular laser cleaning process.

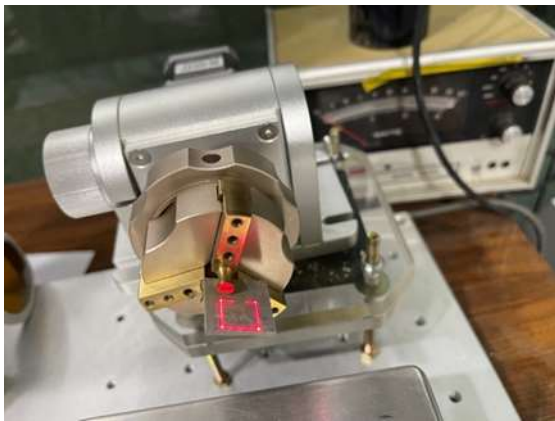


**Fig. 4:** Angular laser cleaning.

**Table 1:** Parameters used in the cleaning process.

Spot size	50,	100,	200
Speed (mm/sec)	Hatch ( $\mu$ m)	Frequency (KHz)	Power (Watt)
150	0.001	20	3
150	0.001	20	5
150	0.001	20	7
150	0.001	20	10

**3. Results and discussion**

**3.1. Microstructure of oxidation layer of aluminium alloy**

For spot size 50  $\mu$ m, figure 5 shows the microstructure of the Al- 4004. Figure 5A illustrate the oxidation layer of Al-4004 while the figures B, C, D, E, F and G illustrated the high damaged on the surface of Al -4004 with the focus spot sizer 50  $\mu$ m with less removed oxidation layer. While spot size 100  $\mu$ m, Figure 6 shows the microstructure of the oxidation layer and the cleaning alloy 4004 at powers of 3, 5, 7, and 10 watts, angles of (5, 10, 15, 20, 25, 30) $^{\circ}$  and hatch sizes of 0.001 micrometers. When looking at the surface that has not been cleaned, the oxygen rich zone can be seen, as seen in Figure 6 A. This region has a high roughness, which indicates that the oxygen layers are co-existing. Oxides and maybe other chemicals, such as hydrocarbon contamination and moisture, are produced by the oxygen-rich region's outermost layer. This layer also contributes to the formation of oxides. Fig 6 B, C and D show that the surface of AL-4004 was only partially cleaned using a dispersion of Si that was not homogeneous. While in Fig. 6 E, F, and G, the power was concentrated on the oxidation layer with a power of 10W and angles of 20, 25, and 30 degrees, the laser power was partially reflected and lost, and a large amount of laser power was absorbed by thin oxidation layer. This caused the temperature in the oxidation layer to increase rapidly, and when the temperature reached or exceeded the vaporization point of the material, phase change occurred, and thus the oxidation layer disappeared. For spot size 200  $\mu$ m, the removed oxidation layer less than 100  $\mu$ m best results shows for angles 15- 25  $^{\circ}$  figures 7 C, D and E.

**3.2. Energy-dispersive X-ray EDX**

In table 2, the chemical composition of AL-4004 was shown. EDS was used for both qualitative and quantitative analysis. After that, the sample was looked at with an XRD to find out what its binary phase composition was.

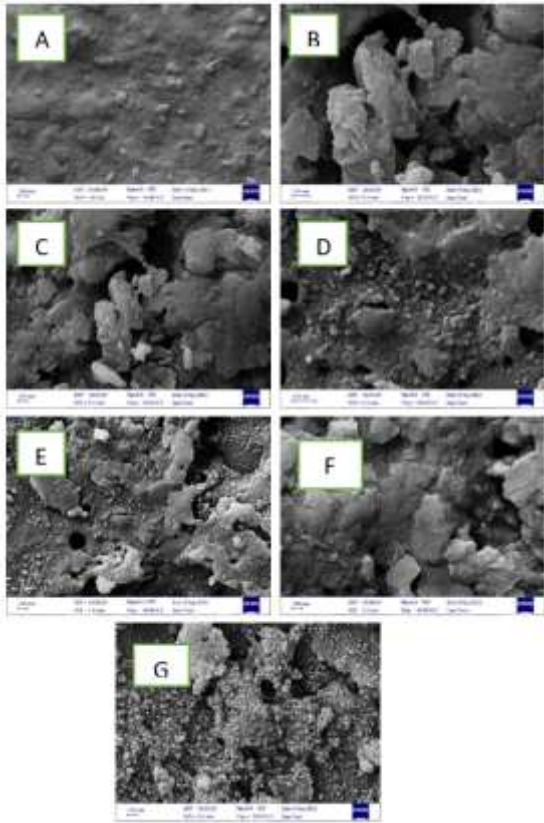


**Fig. 5:** SEM images A. pure oxidation layer, B. Al -4004 with angle laser cleaning 5°, C. Al -4004 with angle laser cleaning 10°, D. Al -4004 with angle laser cleaning 15°, E. Al -4004 with angle laser cleaning 20°, F. Al -4004 with angle laser cleaning 25° and G. Al -4004 with angle laser cleaning 30°.

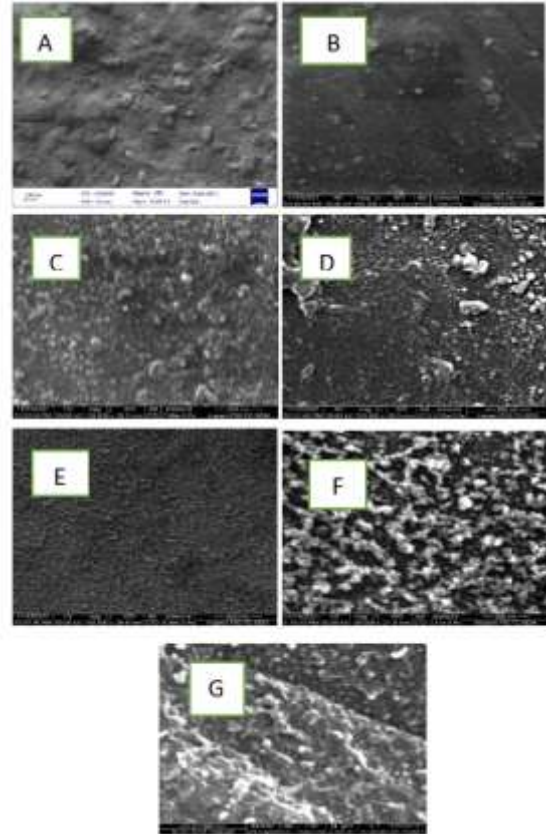


**Fig. 6:** SEM images of spot size 100  $\mu\text{m}$  with power 10W A. pure oxidation layer, B. Al -4004 with angle laser cleaning 5°, C. Al -4004 with angle laser cleaning 10°, D. Al -4004 with angle laser cleaning 15°, E. Al -4004 with angle laser cleaning 20°, F. Al -4004 with angle laser cleaning 25° and G. Al -4004 with angle laser cleaning 30°

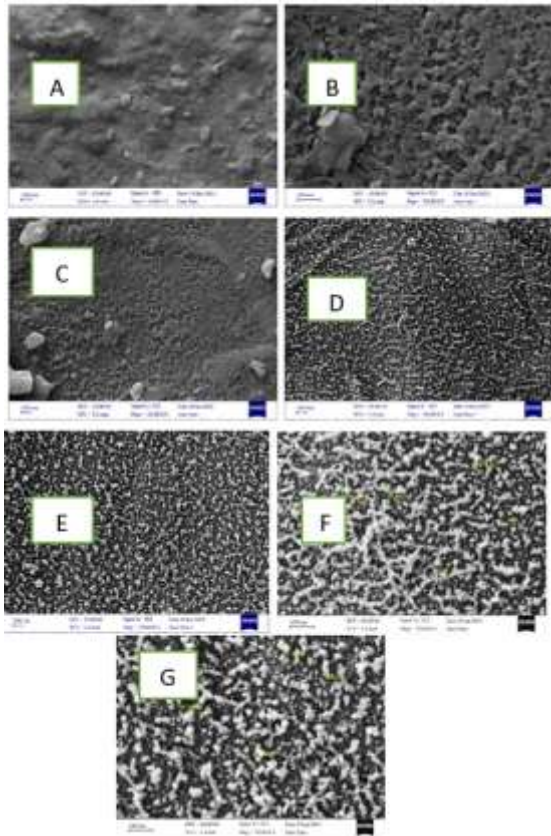


**Fig. 7:** SEM images of spot size 200 μm with power 10W A. pure oxidation layer, B. Al -4004 with angle laser cleaning 5°, C. Al -4004 with angle laser cleaning 10°, D. Al -4004 with angle laser cleaning 15°, E. Al -4004 with angle laser cleaning 20°, F. Al -4004 with angle laser cleaning 25° and G. Al -4004 with angle laser cleaning 30°.

**Table 2:** chemical composition of oxidation layer AL-4004.

Chemical element	Wt.%
Aluminum	48.9
Silicon	6.5
Oxygen	44.6

Following EDS examinations, the atomic composition of oxygen is reduced from 44.8 percent to 42.57 for spot size 50 μm figure 8 best result showed at angle 25 ° with power 10W which was 42.9, while the EDS examinations for spot size 100, the atomic composition of oxygen is reduced from 46.4 percent to 12.88 percent using spot size 100 μm respectively in Fig 9. The result indicated best-removed oxide at hatch 0.001μm with power 10W and for angle 20°. EDS of spot

size 200 μm illustrated at figure 10, the oxygen percentage increased from 45.33 to 45.78 best results showed at angle 20 ° with power 10 W and it was 44.58.

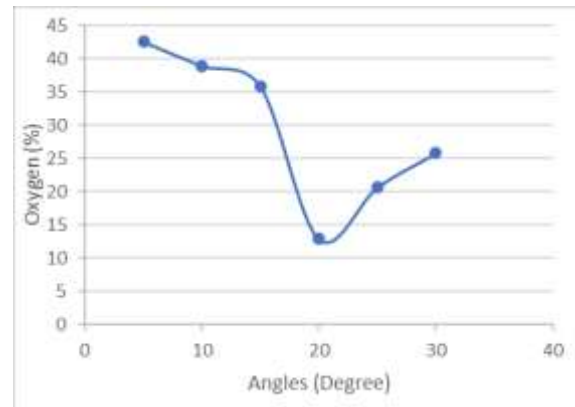


**Fig. 8:** EDX analysis of AL 4004 at angles (5, 10, 15, 20, 25, 30) ° with hatch 0.001 and power 10W and spot size 50 μm.

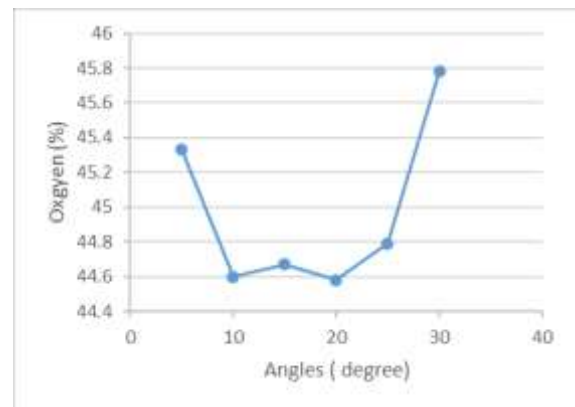


**Fig. 9:** EDX analysis of AL 4004 at angles (5, 10, 15, 20, 25, 30) ° with hatch 0.001 and power 10W and spot size 100 μm.

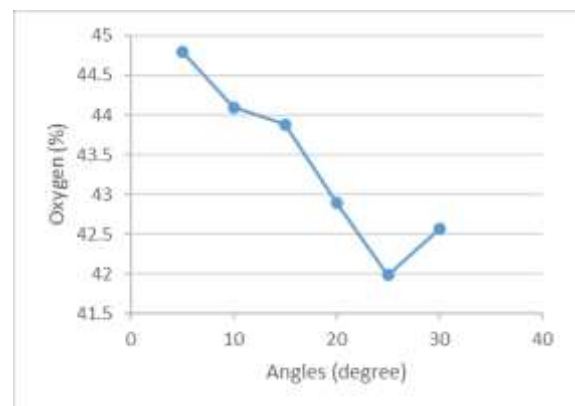


**Fig. 10:** EDX analysis of AL 4004 at angles (5, 10, 15, 20, 25, 30) ° with hatch 0.001 and power 10W and spot size 200 μm.

### 3.3. Roughness and hardness test

The vertical variation that has been measured over a distance is what is meant when we talk about surface roughness. It is possible to define it in a number of different ways, including by the average roughness (Ra), the root mean square roughness (Rq), the height of the roughness profile's highest peak (Rp), and the depth of the roughness profile's deepest valley (Rv), amongst other possible ways. In between these two properties is Rq, which is more closely connected to the optical quality of a surface. Because of this, it is believed that the Rq value is associated to laser cleaning more closely than the other features. In addition, Rv may influence the effectiveness of the laser cleaning. In cases where Rv is high, the oxide layer may function more efficiently. As a result, laser cleaning could be challenging:

$$R_a = \frac{1}{a} \int_{x=0}^a |f(x)| dx \quad (1)$$

Where,  $f(x)$  is the surface height measured from the mean line and 'a' is the total distance that surface roughness is considered. The laser cleaning procedure is affected not only by the adherence of the graffiti, but also by the laser's absorption at the specific laser strength. Increased adhesion will make laser cleaning harder. At the same time, as absorption rises with constant laser power, laser cleaning will be simple. Figures 11, 12 and 13 Shows the roughness test results for spot size 50 -200  $\mu\text{m}$  respectively, and these results revealed that roughness decreased with increasing the laser power and the best impact was at 20° angle for spot size 100  $\mu\text{m}$  while less roughness recorded for spot size 50  $\mu\text{m}$  at angle 10° and power 10W while spot size 200 less roughness illustrated at angle 30°. while for the hardness, as shown in Figures 14, 15, 16 for spot size 50 -200 respectively, these values were selected according to the best distribution of Si. the behaviour of the curves shows that, by increasing the power the hardness value increases, the reason behind such behaviour for aluminum alloy can be explained as follows: first) when laser power density increases, the temperature at the surface metal

increases too, due to the absorption of the laser energy, this increase of the temperature allows the structure of the alloy to be harder. Furthermore, second) the rise in the hardness value with the rise of the power might be due to the melting of the alloy's surface layer, causing decreases of silicon particles size below the critical size to fracture, strengthening the Al-Si alloy [23, 24].

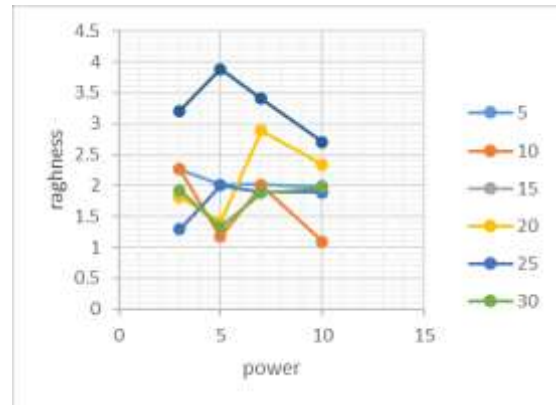


Fig .11: The roughness of different angular angles with different power with spot size 50.

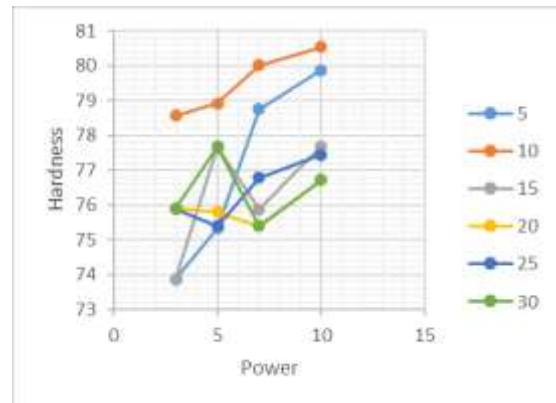


Fig. 12: The roughness of different angular angles with different power with spot size 100.

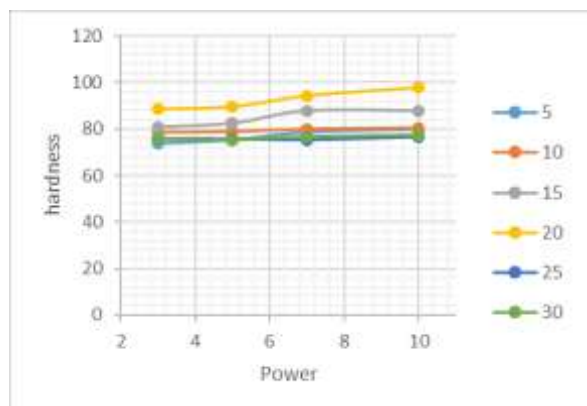


Fig. 13: The roughness of different angular angles with different power and spot size 200.

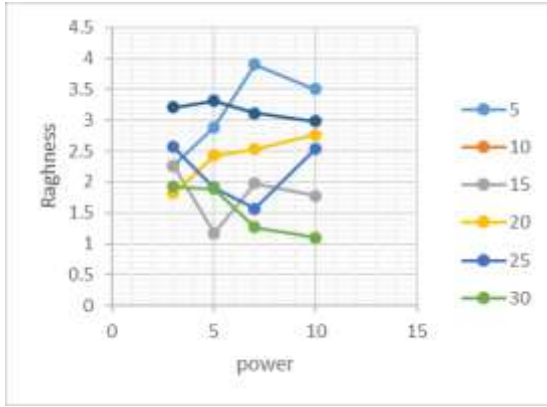


Fig. 14: The hardness of different angular angles with different power and spot size 50.

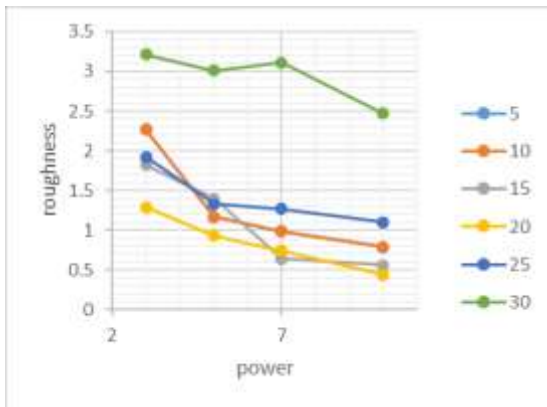


Fig. 15: The hardness of different angular angles with different power and spot size 100.

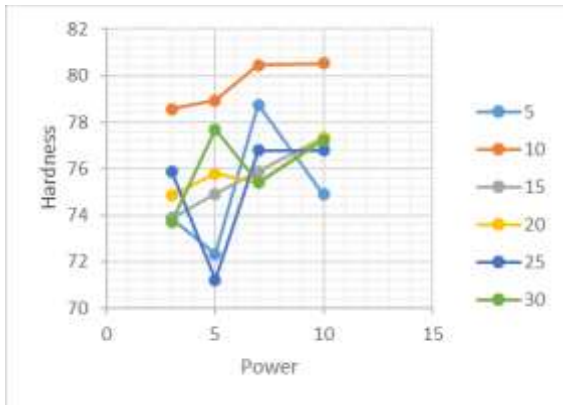


Fig. 16: The hardness of different angular angles with different power and spot size 200.

#### 4. Conclusion

With the help of an angular laser, the oxidation layer was removed from AL-4004 surfaces. Using power 10 W and hatch 0.001, cleaning at an angle of 20° is more effective than cleaning at other angular angles (5, 10, 20, 25, 30) with power 10W especially for spot size 100 μm. The oxidation layer was successfully

eliminated and AL<sub>2</sub>O<sub>3</sub> was reduced by cleaning with hatch 0.001. The roughness decreased as the cleaning angle and power were increased. Hardness was found to rise with increasing amounts of silicon particles on the alloy surface, as well as with the strength and cleaning process used. In order to better understand how the technique works, the adhesion forces and the cleaning forces created by the laser have been taken into account, while at 50 and 200 μm different behaviour of roughness And hardness at angle 10° and 30° .

#### References

- [1] P. Vasantheakumar, K. Sekar, k. Venkatesh, "Recent developments in powder metallurgy based aluminium alloy composite for aerospace applications", Today Proc.vol.18, Mater, 5400–5409. 2019. doi.org/10.1016/j.matpr.2019.07.568
- [2] S. N. Ali, Z. A. Taha, T. S. Mansour, "Laser Cleaning Using Q-Switched Nd:YAG Laser of Low Carbon Steel Alloys", vol. 2014, Advances in Condensed Matter Physics, pp. 6, 2014. doi.org/10.1155/2014/418142
- [3] Y. Ren, L. Wang, J. Li, W, Cheng and X. Ma, "The Surface Properties of an Aviation Aluminum Alloy after Laser Cleaning", vol. 12(2), coatings, 273, 2022. doi.org/10.3390/coatings12020273
- [4] L.Yue, Z. wang, L. Li, "modeling and simulation of laser cleaning of tapered micro – solts with different temporal pulses", Optics and laser technology 45, P. 533- 539, 2013. doi.org/10.1016/j.optlastec.2012.05.036
- [5] Song, M.; Wu, L.; Liu, J.; Hu, Y. "Effects of laser cladding on crack resistance improvement for aluminum alloy used in aircraft skin". Vol. 133Opt. Laser Technol, 10653, 2022. doi:10.1016/j.optlastec.2020.106531
- [6] Y. Ye, Xiaodong Yuan, Xia Xiang, Xiaofeng, Xining Miao, "laser cleaning of particles and grease contamination on the surface of optics", vol. 123 optic, pp. 1056 – 1060, 2012. doi: 10.1088/0256-307X/28/7/074205
- [7] L. Iazzeretti, F. Capone T. Cinti, "open innovation in city of art: the case of laser technology for conservation in Florence ", vol.

- 2, city culture and society, pp.159-168 contents, 2011. doi.org/ 10.1016/ j.ccs. 2011. 09. 001
- [8] L. Lazzeretti R. J. Beach, "the case of laser in conservation of art work in Florence", regional studies association annual international conference, 2010. doi 10.1007/s00339-011-6690-8
- [9] Lammel. C, Dilger. K, Boehm. S, Doerfler. P. "Laser treatment of metal substrates to increase wettability and improve adhesion". Proceedings of the Annual Meeting of the Adhesion Society, p. 217, (2003). DOI:10.1117/12.782989
- [10] Shi T., Wang C., Mi G., Yan F. A study of microstructure and mechanical properties of aluminum alloy using laser cleaning. Vol. 42, J. Manuf. Process, pp. 60–66, 2019. DOI:10.1016/j.jmapro.2019.04.015
- [11] Aamir, M.; Tolouei-Rad, M.; Giasin, K.; Vafadar, A. Feasibility of tool configuration and the effect of tool material, and tool geometry in multi-hole simultaneous drilling of Al2024. Vol. 111, Int. J. Adv. Manuf. Technol. 1–19, 2020. doi.org/10.1007/s00170-020-06151-7
- [12] Samir khudhir al – ani "laser effect on fatigue resistance of carbon steel" Baghdad science journal pp.44-47, 2010. <https://www.iasj.net/iasj/download/ca2f918abf1c48e1>
- [13]. AlShaer, A.W.; Li, L.; Mistry, A. "The effects of short pulse laser surface cleaning on porosity formation and reduction in laser welding of aluminium alloy for automotive component manufacture". Vol. 64, Opt. Laser Technol., 64, 162–171, 2014. doi.org/10.1016/j.optlastec.2014.05.010
- [14]. J.M. Lee, K.G. Watkins, W.M. Steen, Angular laser cleaning for effective removal of particles from a solid surface, Appl. Phys. A 71, 671–674 (2000) doi.org/10.1007/s003390000583
- [15] Barnier, V., et al., "XPS and SIMS study of aluminium native oxide modifications induced by Q-switched Nd : YAG laser treatment", Surface and Interface Analysis, Vol. 38(4): p. 406-409, 2006. doi.org/10.1016/j.matpr.2019.07.568
- [16] G. Zhu , S. Wang , W. Cheng , G. Wang , W. Liu and Yuan Ren, "Investigation on the Surface Properties of 5A12 Aluminum Alloy after Nd: YAG Laser Cleaning", vol. 9, 578, 2019. doi.org/10.3390/coatings9090578
- [17] Zhu, G.; Wang, S.; Zhang, M.; Yang, X.; Liu, W.; Wang, G. "Application of laser cleaning in postwelding treatment of aluminum alloy". Vol. 59, Appl. Opt. 10967–10972, 2020. doi.org/10.1364/AO.406171
- [18] S. Hegde and K.N. Prabhu, Modification of eutectic silicon in Al–Si alloys" vol. 43, J. Mater. Sci. 3009 (2008). doi.org/10.1007/s10853-008-2505-5
- [19] Spot welding of dissimilar metals using automated Nd; YAG laser system TA Tawfiq ZA Taha, Fl Hussein, AA Shehab vol. 11(A) Iraqi journal of laser , 1-5. 2019.
- [20] Zhang Y., Long B., Meng K., Gohkman A., Zhang Z. Diffusion bonding of Q345 steel to zirconium using an aluminum interlayer. Vol. 275 J. Mater. Process. Tech. pp. 2–4, 2019. DOI:10.1016/j.jmatprotec.2019.116352
- [21] Gomes V., Dionísio A., Pozo-Antonio J.S., Rivas T., Ramil A. Mechanical and laser cleaning of spray graffiti paints on a granite subjected to a SO<sub>2</sub>-rich atmosphere. Constr. Build. Vol. 188, Mater, 621–632. 2018 <https://doi.org/10.1364/OE.468750>
- [22] H. Jia, H. Sun, H. Wang, Y. Wu, H. Wang, Scanning strategy in selective laser melting (SLM): a review, The International Journal of Advanced Manufacturing Technology, vol. 113, Iss. 9-10, pp. 2413-2435, 2021. DOI:10.1007/S00170-021-06810-3
- [23] X. Li, D. Wang, J. Gao, W. Zhang, C. Li, Nianzheng Wang, and Yucheng Lei, "Influence of ns-Laser Cleaning Parameters on the Removal of the Painted Layer and Selected Properties of the Base Metal" Materials (Basel), v.13(23); 2020. doi: 10.3390/ma13235363
- [24] L. K.K., H. M.R. "The effects of laser peening and shot peening on fretting fatigue in Ti–6Al–4V Coupons", Tribol. Int. 2009; doi: 10.1016/j.triboint.2009.04.005

## التنظيف الزاوي الليزري لسبيكة المنيوم نوع 4004 بنقاط ليزر مختلفة

زياد اياد طه

ايمان شاكر توفيق\*

معهد الليزر للدراسات العليا/جامعة بغداد

### الخلاصة

عندما يتعلق الامر بالتطبيقات والقطع وهندسة الاسطح، فأن استخدام حزم الألياف عالية الطاقة من ليزر الحالة الصلبة يوفر العديد من الفوائد. يتضمن هذا البحث تنظيف الاسطح بنقاط ذات احجام مختلفة (50، 100، 200) مايكرومتر (ليزر الألياف الإيترييوم الصناعي) لتجهيزها للحام. تم استخدام التنظيف بالليزر بالزوايا التالية (5، 10، 15، 20، 25، 30)° وبقدرات مختلفة (3، 5، 7، 10) وات ومساحة التنظيف 0.001



## Lab-On-a-Chip an integrated microfluidic device sensitive low-Cost, and Rapid with a syringe pump for Analysis of Ibuprofen

Huda S. Ezzat<sup>1</sup> and Rawaa A. Faris<sup>1,\*</sup>

\*Corresponding author: [Rawaa@ilps.uobaghdad.edu.iq](mailto:Rawaa@ilps.uobaghdad.edu.iq)

1- Institute of Laser for Postgraduate Studied, University of Baghdad, Baghdad, Iraq.

(Received 19/10/2022; accepted 29/01/2023)

**Abstract:** Microfluidic devices present unique advantages for the development of efficient drug assay and screening. The microfluidic platforms might offer a more rapid and cost-effective alternative. Fluids are confined in devices that have a significant dimension on the micrometer scale. Due to this extreme confinement, the volumes used for drug assays are tiny (milliliters to femtoliters).

In this research, a microfluidic chip consists of micro-channels carved on substrate materials built by using Acrylic (Polymethyl Methacrylate, PMMA) chip was designed using a Carbon Dioxide (CO<sub>2</sub>) laser machine. The CO<sub>2</sub> parameters have influence on the width, depth, roughness of the chip. In order to have regular channel surface, and low roughness the laser power (60 W), with scanning speed (250 m/s) for allows us to obtain microchannels with a minimum diameter of width (450 μm), depth of the channels was 89.4 μm and( Arithmetic Average Roughness Ra = 2.3), (Relative roughness,  $\mathcal{E} = 5\%$ ) surface roughness with high accuracy and good surface quality.

The functionalized multiwalled carbon nanotubes (F-MWCNTs) was used to enhance the drug signal in order to detect very tiny Ibuprofen concentration. In this work, laser microfluidic sensor have high accuracy in Ibuprofen detection compared to the traditional method(UV-VIS) spectrophotometer with LOD equal to 0.25 nM, 1000μM respectively.

**Keywords:** microfluidic chip, syringe pump, acrylic, Ibuprofen, grbl laser program, diode laser (532m).

### Introduction

Microfluidics is a field of science studying fluids (i.e., liquids and gasses) on a microscopic scale. Therefore, fluids are confined in devices that have a significant dimension (e.g., the height or the width) on the micrometer scale[1-4]. Due to this extreme confinement, the volumes used for drug assays and similar studies are tiny (milliliters to femtoliters), and special physics apply. In short, in a microfluidic device there are only laminar flows and no turbulences, which grants an extremely high control over the fluids employed, diffusion of drugs and the progress of reactions [ 5-9]. Several types of microfluidic penetrate into these micro channels,

and then some of these fluids are stored in the micro channels. Then, these fluids are combined with the mixers and create a specific reaction. Finally, the final product of this reaction will come out of the machine. The function of this device can be checked by ultraviolet microscopes, etc. Microfluidic systems have vast applications that have widespread use of the system in medicine and biology, as well as in research and laboratory. The technology of lab on a chip (LOC) is one of the applications of these systems that part of the chip acts as a part of the lab. The benefits of this technology include high sensitivity, isolation, reduced time and cost, high reparability and excellent detection[10-13]. Materials of the Chip Silicon and glass are the



roughness of the channel. The fabrication process of the PMMA based microfluidic chips. Thirdly, the PMMA substrate, was been covered with an epoxy resin used as an adhesives, then the PMMA

substrate was attached to another layer of PMMA,(same material and same thickness) containing holes (Two inlets,and one outlet), finally, to seal off the manufactured microchannels. The pipes for inlets and outlet ports then connected to the holes to finish the fabrication process.of the microfluidic chip.

Inlets, and one outlet), finally, to seal off the manufactured microchannels. The pipes for inlets and outlet ports then connected to the holes to finish the fabrication process.of the microfluidic chip.

The construction of the syringe pump system needed electrical and mechanical engineering. Colorful models and circuits were estimated in order to find the stylish design for the below reasons. The custom corridor for the injection pump were created using SolidWorks design software. Cura software was used in 3D printing test models of designs on a regular direct printer. In order to produce completely cohesive pieces, accurate measures were needed. Figure (2a) shows the Solid Work assembly of a single syringe pump model with all corridors planned. The first type was put through its paces to insure it had a solid frame and moved easily. Figure2 (b) depicts the picture of the fabricated syringe pump.

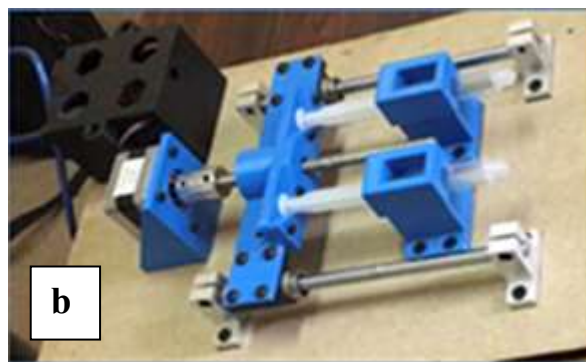
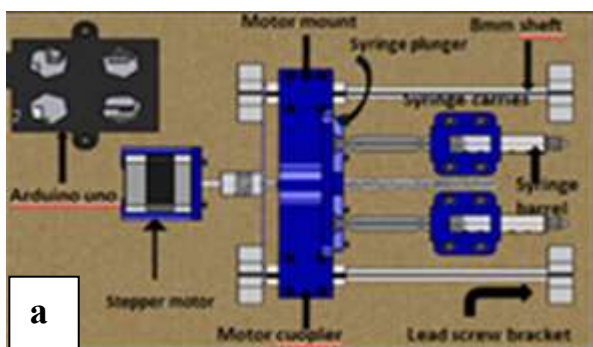


Fig. 2: (a) Solid Works design software 3D model assembly of a double syringe pump (b) fabricated syringe pump assembled with Nema 17 motor and 5mL syringe

Figure (3) shows the constructed laser microfluidic sensor, which consist of diode laser(532nm,20 mW),lens) focal length 1.5 mm),detector from UNO, Gentec, PH100 & PH20 series, china, fabricated double syringe pump to provide the pumping of F-MWCNTs and Ibuprofen ,microfluidic chip and PC. In this sensor the standard solution of Ibuprofen.

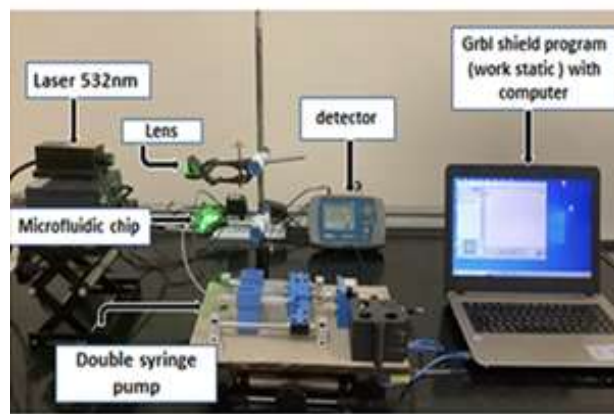


Fig. 3: Set up of laser microfluidic sensor

## 2.2. Standard solutions

Stock solutions of 1 mg/ml of IB were prepared by dissolving 100 mg of IB in 100 ml water. The solutions were prepared by dilution of the stock solutions with the same solvent to reach concentration range (250, 500,1000, 4000, 7000, 9000)  $\mu$ M.

### 3. Result and Discussion

#### 3.1. Characterization of Microfluidics Chip

In Figure 4(a), microscope images of the microfluidic chip fabricated by laser ablation. Channels produced using laser ablation exhibited a regular shape and clean ablation edge. The channel width 450  $\mu\text{m}$  with associated uneven topography. Since PMMA has a relatively low thermal diffusivity, the intensity distribution mostly defines the channel profile. The microchannel has a Gaussian-shaped profile as a result of laser beam's energy being distributed Gaussianly.

A pool of molten polymer is formed on the workpiece surface where the laser beam makes contact with it as it advances over the surface. The heated gas of the vaporizing polymers drives the pool away from the hot point in all directions, while the majority of the melted material re-solidifies in the aftermath of the beam, leaving behind minor bumps on the

microchannel's borders. The surface roughness of the laser ablated microfluidic chips was also measured with the help of the laser confocal microscope. Figure 3( b) shows the laser confocal microscope image of the laser-ablated microchannel with a laser power of 60 watt and a travel speed of 250mm/s. The surface roughness was measured at the inner wall of the fabricated microchannels ( Arithmetic Average Roughness  $R_a = 2.3$ ), (Relative roughness,  $\epsilon = 5\%$ ) surface roughness with high accuracy and good surface quality.

Also, the laser confocal microscope used to find the depth of the channels which is equal to 89.4 $\mu\text{m}$ .

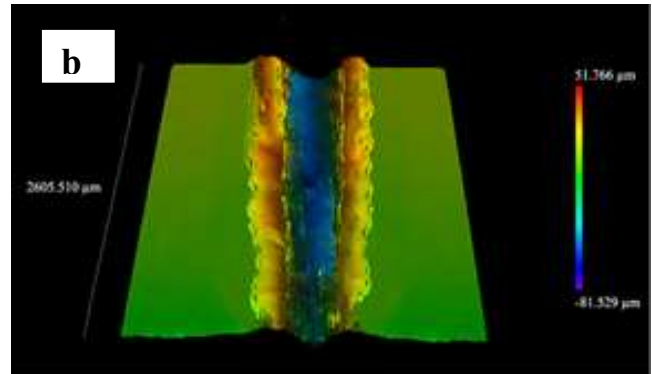


**Fig. 4:** (a) Showing width of the microfluidic chips via the optical microscope images at power of laser is constant at 60watt & travel speed is 250 mm/s (b) Showing the depth of the microfluidic chips via Confocal Laser Scanning Microscope.

#### 3.2. Determination of Ibuprofen concentration using the constructed laser microfluidic sensor

Microfluidic chip irradiated by Diode lasers (532nm) at 100 mW by programming the double syringe pump using Grbl software.

The value of the incident beam on the solution was obtained inside an acrylic (PMMA) microfluidic channel, and the result was displayed by (Uno laser power meter mW). The intensity is inversely proportion with the increasing in concentration.

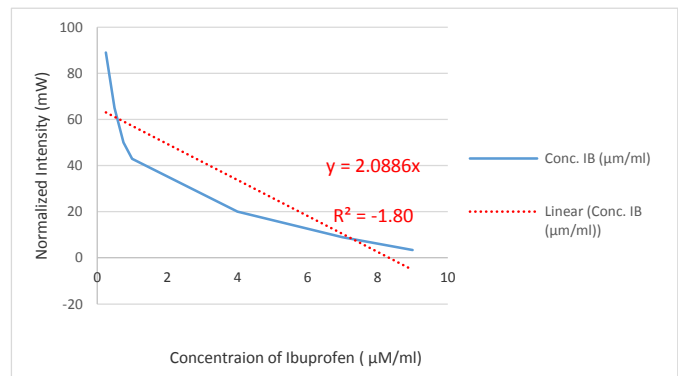


**Fig. 5:** Calibration curve of Ibuprofen as estimated from laser microfluidic sensor

Then these results were compared with the results from UV-VIS. Figure (6) represented the calibration curve of Ibuprofen that extracted from UV-VIS spectrophotometer.

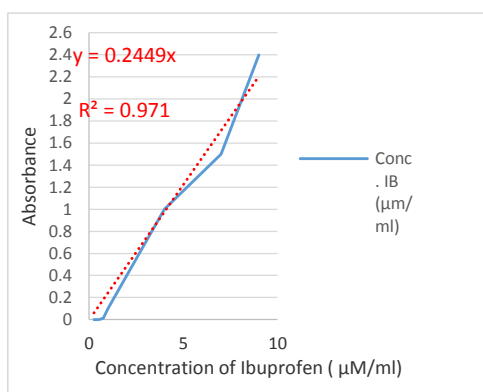


**Fig. 6:** calibration curve of Ibuprofen from UV-VIS spectrum

From figures 5& 6 the precision, recovery, linearity, and LOD can be extracted as listed in table 1

**Table (1):** Parameters of the two analytical methods to determine IB concentration

parameters	Laser microfluidic sensor	Uv-vis
Correlation coefficient ( $R^2$ )	<b>1.801</b>	<b>0.97</b>
LOD ( $\mu\text{g/mL}$ )	<b>0.25</b>	<b>1</b>
Recovery	<b>99.7</b>	<b>98.5</b>
linearity	<b>0.25-9</b>	<b>1-9</b>

#### 4. Conclusion

As a new platform, microfluidic instruments offer a lot of potential. More than 20 years ago, microfluidic technologies started to make a difference in biological research. Microfluidic devices have a lot of potential. Studies have shown that it is a developing Microfluidics technology. Owing to their high throughput, great sensitivity, and low cost, is invaluable for research, cost, reduced material usage, and enhanced spatiotemporal control. Additionally, portable microfluidic equipment is available.

#### References

[1] Shembekar, N.; Chaipan, C.; Utharala, R.; Merten, C.A. Droplet-based microfluidics in drug discovery, transcriptomics and high-throughput molecular genetics. *Lab Chip* 2016, 16, 1314–1331. [CrossRef] [PubMed]  
 [2] Fontana, F.; Ferreira, M.P.A.; Correia, A.;

Hirvonen, J.; Santos, H.A. Microfluidics as a cutting-edge technique for drug delivery applications. *J. Drug Deliv. Sci. Technol.* 2016, 34, 76–87. [CrossRef]  
 [3] Tsui, J.H.; Lee, W.; Pun, S.H.; Kim, J.; Kim, D.-H. Microfluidics-assisted in vitro drug screening and carrier production. *Adv. Drug Deliv. Rev.* 2013, 65, 1575–1588. [CrossRef] [PubMed]  
 [4] Riahi, R.; Tamayol, A.; Shaegh, S.A.M.; Ghaemmaghami, A.M.; Dokmeci, M.R.; Khademhosseini, A. Microfluidics for advanced drug delivery systems. *Curr. Opin. Chem. Eng.* 2015, 7, 101–112. [CrossRef]  
 [5] Du, G.; Fang, Q.; den Toonder, J.M.J. Microfluidics for cell-based high throughput screening platforms-A review. *Anal. Chim. Acta* 2016, 903, 36–50. [CrossRef] [PubMed]  
 [6] Junkin, M.; Tay, S. Microfluidic single-cell analysis for systems immunology. *Lab Chip* 2014, 14, 1246–1260. [CrossRef] [PubMed]  
 [7] Clausell-Tormos, J.; Lieber, D.; Baret, J.-C.; El-Harrak, A.; Miller, O.J.; Frenz, L.; Blouwolff, J.; Humphry, K.J.; Köster, S.; Duan, H.; et al. Droplet-based microfluidic platforms for the encapsulation and screening of mammalian cells and multicellular organisms. *Chem. Biol.* 2008, 15, 427–437. [CrossRef] [PubMed]  
 [8] Theberge, A.B.; Courtois, F.; Schaerli, Y.; Fischlechner, M.; Abell, C.; Hollfelder, F.; Huck, W.T.S. Microdroplets in microfluidics: An evolving platform for discoveries in chemistry and biology. *Angew. Chem. Int. Ed.* 2010, 49, 5846–5868. [CrossRef] [PubMed]  
 [9] Guo, M.T.; Rotem, A.; Heyman, J.A.; Weitz, D.A. Droplet microfluidics for high-throughput biological assays. *Lab Chip* 2012, 12, 2146–2155. [CrossRef] [PubMed]  
 [10] Rogers CI, Qaderi K, Woolley AT, et al. 3D printed microfluidic devices with integrated valves. *Biomicrofluidics*. 2015;9(1):016501.  
 [11] Sajeesh P, Kumar Sen A. Particle separation and sorting in microfluidic devices: a review. *Microfluid Nanofluid*. 2013;17(1):1–52.  
 [12] Pinho D, Rodrigues RO, Faustino V, et al. Red blood cells radial dispersion in blood flowing through microchannels: The role of temperature. *J Biomech*. 2016;49(11):2293–2298.  
 [13] Ahmadian Yazdi A, Popma A, William Wong, et al. 3D printing: an emerging tool for novel microfluidics and lab-on-a-chip applications. *Microfluidics and Nanofluidics*. 2016;20:50.  
 [14] Mcdonald, J.C.; Duffy, D.C.; Anderson, J.R.;

- Chiu, D.T.; Wu, H.; Schueller, O.J.A.; Whitesides, G.M. Fabrication of microfluidic systems in poly(dimethylsiloxane). *Electrophoresis* 2005, 21, 27–40. [CrossRef]
- [15] Cai, J.; Jiang, J.; Gao, F.; Jia, G.; Zhuang, J.; Tang, G.; Fan, Y. Rapid prototyping of cyclic olefin copolymer based microfluidic system with CO laser ablation. *Microsyst. Technol.* 2017, 23, 5063–5069. [CrossRef]
- [18] Valentin, T.M.; Leggett, S.E.; Chen, P.Y.; Sodhi, J.K.; Stephens, L.H.; McClintock, H.D.; Sim, J.Y.; Wong, I.Y. Stereolithographic printing of ionically-crosslinked alginate hydrogels for degradable biomaterials and microfluidics. *Lab Chip* 2017, 17, 504–523. [CrossRef].
- [19] Schuler, T., Asmus, T., Fritzsche, W. and Moller, R. (2009). Screen printing as cost-efficient fabrication method for DNA-chips with electrical readout for detection of viral DNA. *Biosens Bioelectron*, 24, 2077–84. DOI 10.1016/j.bios.2008.10.028
- [20] Schulze, M. and Belder, D. (2012). Poly(ethylene glycol)-coated microfluidic devices for chip electrophoresis. *Electrophoresis*, 33, 370–8. DOI: 10.1002/elps.201100401].
- [21] Ebeshi, B.U.; Oseni, K.E.; Ahmadu, A.A.; Oluwadiya, J.O. Comparative utilization of
- [16] Kim, A.A.; Kustanovich, K.; Baratian, D.; Ainla, A.; Shaali, M.; Jeffries, G.D.M.; Jesorka, A. SU-8 free-standing microfluidic probes. *Biomicrofluidics* 2017, 11, 014112. [CrossRef]
- [17] Yamada, K.; Shibata, H.; Suzuki, K.; Citterio, D. Toward practical application of paper-based microfluidics for medical diagnostics: State-of-the-art and challenges. *Lab Chip* 2017, 17, 1206–1249. [CrossRef]
- visual, potentiometric titrations and UV spectrophotometric methods in the determination of ibuprofen. *Afr. J. Pharm. Pharmacol.* 2009, 3, 426–431.
- [22] Dolowy, M. Influence of different chromatographic conditions on the level of detection and quantitation of spironolactone by means of TLC-densitometry. *J. Anal. Methods Chem.* 2019, 2019. [CrossRef] [PubMed]
- [23] Gentili, A.; Caretti, F.; Bellante, S.; Mainero Rocca, L.; Curini, R.; Venditti, A. Development and validation of two multiresidue liquid chromatography tandem mass spectrometry methods based on a versatile extraction procedure for isolating non-steroidal anti-inflammatory drugs from bovine milk and muscle tissue. *Anal. Bioanal. Chem.* 2012, 404, 1375–1388. [CrossRef] [PubMed].

## بناء جهاز موانع جزيني متكامل حساس ومنخفض التكلفة وسريع مع مضخة حقن

### لتحليل الإيبوبروفين

هدى ساكن عزت  
رواء احمد فارس  
جامعة بغداد/ معهد الليزر للدراسات العليا

**الخلاصة:** تقدم أجهزة ميكروفلويديك مزايا فريدة لتطوير مقاييس وفحص الأدوية بكفاءة. قد توفر منصات ميكروفلويديك بديلاً أكثر سرعة وفعالية من حيث التكلفة. تنحصر السوائل في الأجهزة التي لها أبعاد كبيرة على مقياس ميكرومتر. بسبب هذه الأبعاد الصغيرة، فإن الأحجام المستخدمة في فحوصات الأدوية صغيرة (مليتر إلى فيمتولتر). في هذا البحث، تتكون شريحة ميكروفلويديك من قنوات ميكروية منحوتة على مواد ركيزة مبنية باستخدام شريحة أكريليك (بولي ميثيل ميثاكريلات، PMMA) تم تصميمها باستخدام آلة ليزر ثاني أكسيد الكربون (CO<sub>2</sub>). تؤثر معلمات ثاني أكسيد الكربون على عرض وعمق وخشونة الرقاقة. من أجل الحصول على سطح قناة منتظم، وخشونة منخفضة، قوة الليزر (60 واط)، مع سرعة مسح (250 م / ث) للسماح لنا بالحصول على قنوات صغيرة بقطر أدنى من العرض (450 ميكرومتر)، وكان عمق القنوات 89.4 ميكرومتر و (متوسط الخشونة الحسابي Ra = 2.3)، (الخشونة النسبية، %E = 5) للسطح بدقة عالية وجوده سطح جيدة. تم استخدام الأنابيب النانوية الكربونية متعددة الجدران الوظيفية (F-MWCNTs) لتعزيز إشارة الدواء من أجل اكتشاف تركيز الإيبوبروفين القليل جداً. في هذا العمل، يتمتع مستشعر الموانع الدقيقة بالليزر بدقة عالية في الكشف عن الإيبوبروفين مقارنة بمقياس الطيف الضوئي بالطريقة التقليدية (UV-VIS) مع LOD يساوي 250 نانومتر، 1 ميكرومتر على التوالي.



## Sensing and differentiation between normal flora and pathogenic of *E.coli* Bacteria using 410 nm diode laser

Thair F. A. Al-Khozaee<sup>1,\*</sup> Lyla M. H .Al-ameri<sup>1</sup>

\*Corresponding author: [thaer.farhan1202a@ilps.uobaghdad.edu.iq](mailto:thaer.farhan1202a@ilps.uobaghdad.edu.iq)

1. Institute of Laser for Postgraduate Studies, University of Baghdad, Baghdad, Iraq.

(Received 31/10/2022; accepted 30/01/2023)

**Abstract: Background:** Optical biosensors offer excellent properties and methods for detecting bacteria when compared to traditional analytical techniques. It allows direct detection of many biological and chemical materials. Bacteria are found in the human body naturally non-pathogenic and pathologically, as they are found in other living organisms. One of these bacteria is Escherichia coli (*E. coli*) which are found in the human body in its natural and pathogenic form. *E.coli* bacteria cause many diseases, including Stomach, intestines, urinary system infections, and others. **The aim of this study:** is sensing and differentiation between normal flora and pathogenic *E.coli*. **Material and method:** The optical biosensor constructed of a multi-mode – no core- multi mode optical fibre that differentiates between pathogenic and non-pathogenic bacteria of *E.coli* by measuring the changing for light intensity using source of light 410nm laser diode. Multi-mode - no core - multi-mode optical fibre (MM-NOC-MM) connected to the OSA analyser (HR2000) by means of an adapter and finally connected to a computer to show the results. **Results:** The intensity of the transmitted light recorded in the case of pathogenic bacteria is less than the intensity of the transmitted light recorded in the case of non-pathogenic bacteria. **Conclusion:** these results were obtained because of the ideal and better choice of the wavelength of the laser used with its absorption *E.coli* bacteria.

### Introduction

Normal flora are the microorganisms that live on the surface or inside another living organism (human or animal) or inanimate object without causing disease ((Wang et al., 2017)). Sometime it is called commensal because of their permanent presence on body surfaces even if covered by epithelial cells and are even exposed to the external environment (e.g., respiratory and gastrointestinal tract, genital, hair, etc.) ((Dekaboruah et al., 2020)). Normal flora plays an important role in immunity and inflammation. Significance of the normal Flora for their host is very important. They directly influences the anatomy, physiology,

immunology, even susceptibility to true pathogenic organisms, and even morbidity-mortality of the host; in short terms, it affects the homeostasis of their host (Best et al., 2019). Microbial normal flora has spatio-temporal involvement that differs individually, regional body niche, age, geographical location, health condition, diet and also by type of host ((Lloyd-Price et al., 2016)).

Pathogenic bacteria: The oldest bacterial pathogens in microbiological strain collections date from the 1890s, soon after medical bacteriology was introduced Pathogenic microorganisms cause various

infectious diseases and even death. Despite early triumphs over infectious diseases with the development of vaccines and antibiotics, new and multidrug-resistant pathogens are continuously emerging (Yoo & Lee, 2016).

***Escherichia coli (E. coli)*** *Escherichia coli* is a facultative anaerobic microorganism found in the gastrointestinal tract of warm-blooded animals, with which it maintains a mostly symbiotic relationship. *E. coli* has also been found in soil, water, and sediments not directly influenced by sewage discharges. Besides commensal strains, there exist also pathogenic variants of *E. coli*, capable of causing either intestinal or extra intestinal diseases. Pathogenic strains were probably derived from commensal strains following the horizontal acquisition of chromosomal and extrachromosomal genes and operons, as well as gene loss (Tallon et al., 2005; Whitman et al., 2006; Tenailon et al., 2010) Some *E. coli* strains can cause a wide variety of intestinal and extra-intestinal diseases, such as diarrhea, urinary tract infections, septicemia, and neonatal meningitis (Clermont et al., 2000) Phylogenetic analyses have shown that *E. coli* strains fall into four main phylogenetic groups (A, B1, B2, and D) and that virulent extra-intestinal strains belong mainly to group B2 and B1, to a lesser extent, to group D, whereas most commensal strains belong to group A. These studies have also given us a better understanding of how pathogenic strains acquire virulence gene. *E. coli* is one of the most important and prevalent bacterial types in causing urinary tract infections in

women, and it constitutes more than 80% of pathogens because it is a natural plant inside the human body. From sticking to the epithelial lining of the urinary tract, these bacteria have the ability to survive and gather for a long time inside the urinary tract of the host to be able to avoid the body's immune response and resistance to antibiotics and make it capable of causing repeated infections of the urinary tract (Journal, 2014). **Biosensor:** A biosensor is a device that contains a biological sensing element that is closely associated or integrated with a transducer. The common aim is to produce a digital electronic signal that is proportional to the concentration of a particular chemical or set of chemicals. ((Shatti & Al-ameri, 2021)) The seemingly bizarre connection of two opposing disciplines combines the specificity and sensitivity of biological systems with the computing power of the microprocessor. This emerging technology transcends many traditional academic frontiers and offers a powerful new tool that threatens to radically change the way we think about analytical science. (Pandey and Malhotra 2019) In general, biosensors consist of a bio receptor, the recognition element responsible for capturing the target analyse, and a transducer, the properties of which are modified by the binding of the analyse as shown in figure (1). (Peltomaa et al. 2018) The biological component of a biosensor used for molecular detection consists of highly specialized macromolecules or complex systems with corresponding selectivity and sensitivity. Biosensors can be classified according to the bio components used for detection. (Hossain and Mansour 2019).

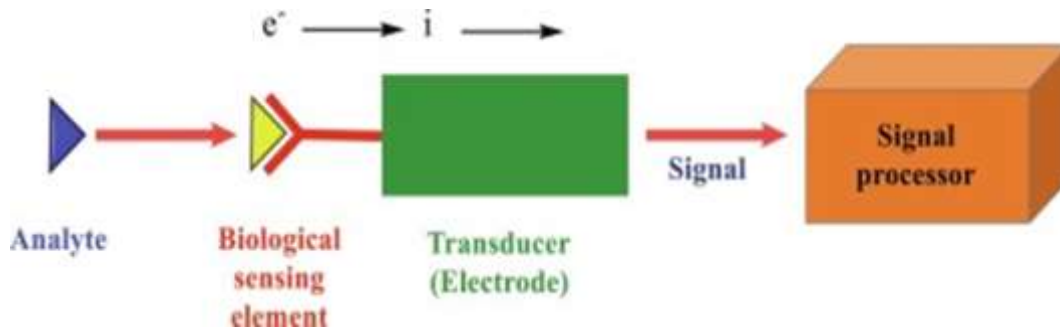


Fig. 1: Biosensor system detection ((Saleh, 2020)

Types of Biosensors: Biosensor is classified according to:

1. Bio-element (Molecular, Cell-based, Tissue-based)
2. Transducer (Optical, Mechanical, Electrochemical)

3. Principle of operation (Fluorescence, Surface plasma resonance, Absorbance\reflectance, Piezoelectric, Surface acoustic wave, Cantilever resonance frequency, Amperometric, Potentiometric, Impedimetric (Alageedi & Alameri, 2019) as shown in the figure (2).

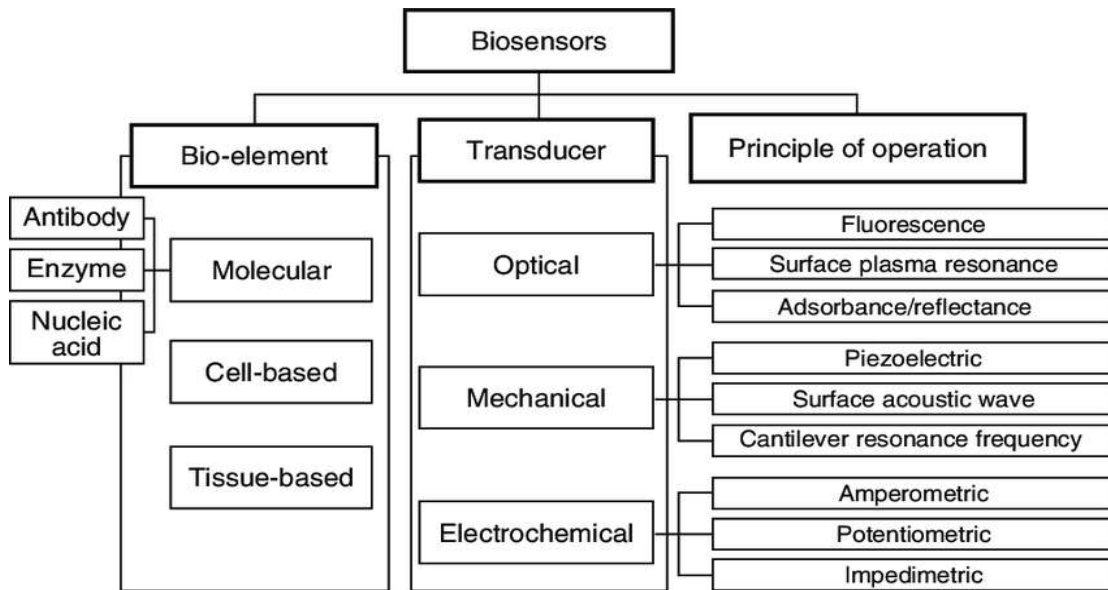


Fig. 2: Types of biosensors (Salam & Alabd, 2019)

In general, optical sensors can be distributed into four classes based on changing in light parameters such as

polarization modulation intensity modulation, wavelength modulation, and phase modulation.( Alameri et al. 2020)

**Basic Design of the Optical Biosensor**

consisting of:

- A. Light source (LED, laser, and other types).
- B. An Optical fibre.
- C. The sensing element (translating the measured into optical signal).
- D. Optical detector and electronic processing (spectrum analyzer, oscilloscope, etc.).

optical systems have: been an important target by many researchers. Because, it has been applied in many fields. Optical fibres are uses in different applications like fibre sensing, spectroscopic analysis, optical fibre laser, and optically filtering. (Kareem & Mansour, 2022)

**Material and Method:** Samples were collected from a group of patients in Al-Diwaniyah Teaching Hospital with diarrhea, intestinal infections and urinary tract infections, as well as from a group of healthy people. The probes were taken, sterilized, and taken to the laboratory. They were cultured on special and differential culture media and incubated at 37°C for 18-24 h.

Subsequently, biochemical and antibiotic sensitivity tests were performed as well as the Vitec 2 device to confirm the diagnosis

**Table(1):** showing biochemical test for E.coli bacteria

Lactose fermenting MacConkey agar	Blood agar	Gram stain	oxidase	catalase	urea's	indole	Methyl red	citrate
+	variable	- ve	-	+	-	+	+	-

**The Optical Biosensor Setup:**

1- multimode- no core - multimode optical fibre 40cm in length was considered as the conventional optical fiber, a segment about 3 cm in length was made in the middle of the fibre(no core fibre) using a cutter to make .finally using hydrofluoric acid 40% for 20 min to etching the cladding so that the diameter of the optical fiber after etching becomes 75 μm by viewing and measuring it under a microscope ding (A small drop of the bacterial solution is placed on it to detect and differentiate the bacteria) .

2- The whole fibre (40) cm was put on the plate using a adhesive.

3- The two ends of fiber were connected with an adapter device

An adapter is used for connecting the optical fiber with the laser from one side and the spectrum analyzer (OSA) from the other side. standard type connectors such as FC, SC, ST, LC, MTRJ, or SMA

4- First end connected with laser source (diode laser) power supply. The light source had been used in this experiment was Blue laser with  $\lambda= 410\text{nm}$  and output power = 40 mw .This source of laser has a power supply which is stable at all the time of use it. Selecting this light source was because the absorption spectra of the bacteria samples covered this wavelength

5- The second end connected with spectrometer (ocean HR2000) and computer to obtain signal of intensity as shown in figure An optical spectrum analyzer (ocean optics HR2000) with

(0.065nm) resolution was used to display transmission interference spectrum of the sensor.

The spectrometer type (ocean optics HR2000), have the following characteristics:

Operating in the wavelength range from 200nm to 1100nm

-Resolution are 0.065nm of the high wavelength

-At full signal, the signal-to-noise – ratio are 250:1

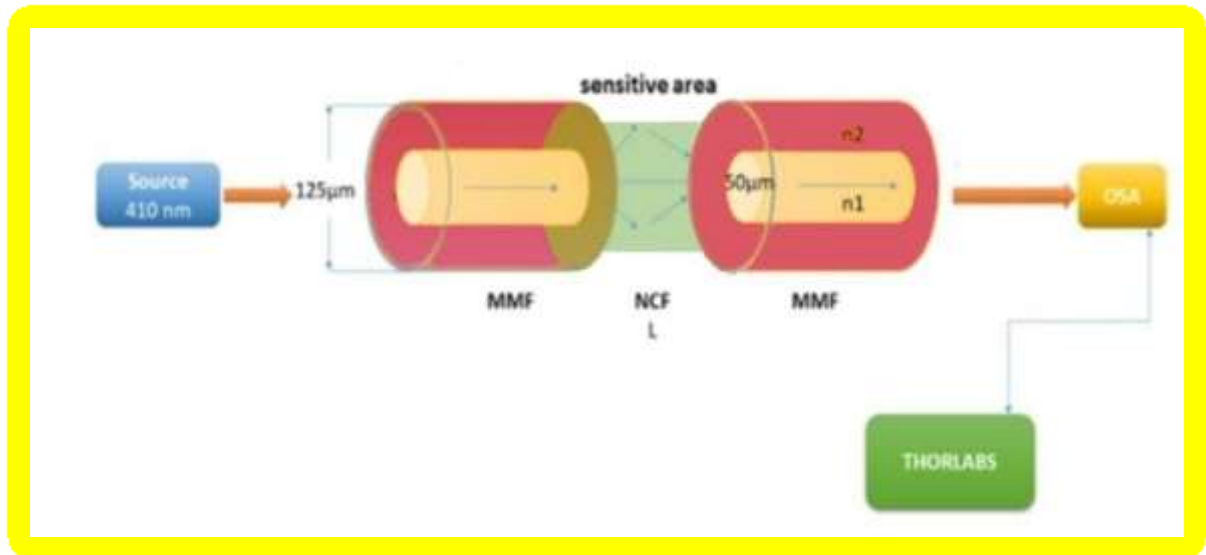


Fig. 3: Basic Elements of a Fiber Optic Sensor(Lang et al., 2019)

### Statistical analysis:

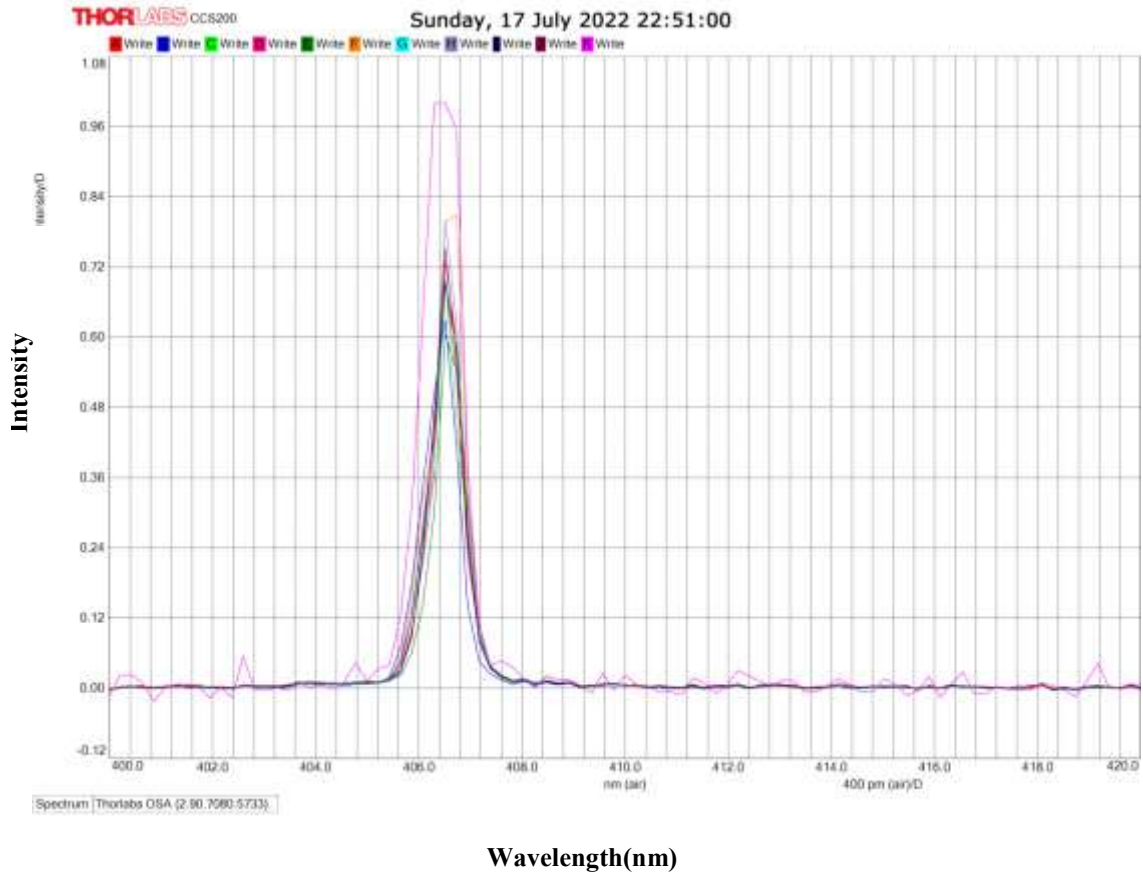
The data were analysed using the Microsoft Excel 2021 and Statistical Package for Social Sciences (SPSS IBM-version 26.0) software. The results reported in this study were expressed as mean  $\pm$  SD (Standard Deviation) and frequencies were expressed as percentages on tables and graphs. Chi-square, independent T-test, and ANOVA were used to examine the degree of significance. Probability values (p-value) less than 0.05 were regarded as significantly different while probability values less than 0.01 were regarded as highly significant .

### Result and discussion:

Biological measurement The positive and negative biochemical tests that were performed on the bacterial colonies of E.coli can be seen as shown in Table (1). The laser intensity of normal and pathogenic E.coli was measured by the sensor MM.NOC.MM as shown in Table ( 2, 3). Through the shape of the peaks, we can see the unique shape of the peak of laser intensity according to the type of fibre used, the absorption of bacteria to laser wavelength and the laser source used(410nm). Through the study, it was found that the laser intensity measurement of pathogenic E.coli bacteria is less than that of non-pathogenic E.coli bacteria due to the higher absorption of pathogenic bacteria because it contains virulence factors, as shown in the figure(4) and figure(5)

Table 2 (pathogenic E.coli): Show results of sample intensity, Peak wavelength nm (air), FWHM(pm)air).

Sample no	Intensity	Peak wavelength nm (air)	FWHM (pm)air
Source	1.000000	406.0802002	820.1606058
1	0.6932	406.5158	447.0406
2	0.6301	406.5158	772.9235
3	0.7026	406.5158	662.4109
4	0.7295	406.5158	587.2161
5	0.6036	406.5158	671.4633
6	0.8087	406.7337	661.1219
7	0.6848	406.5158	658.2355
8	0.7995	406.5158	634.9289
9	0.6937	406.5158	700.9178
10	0.7523	406.5158	661.4069

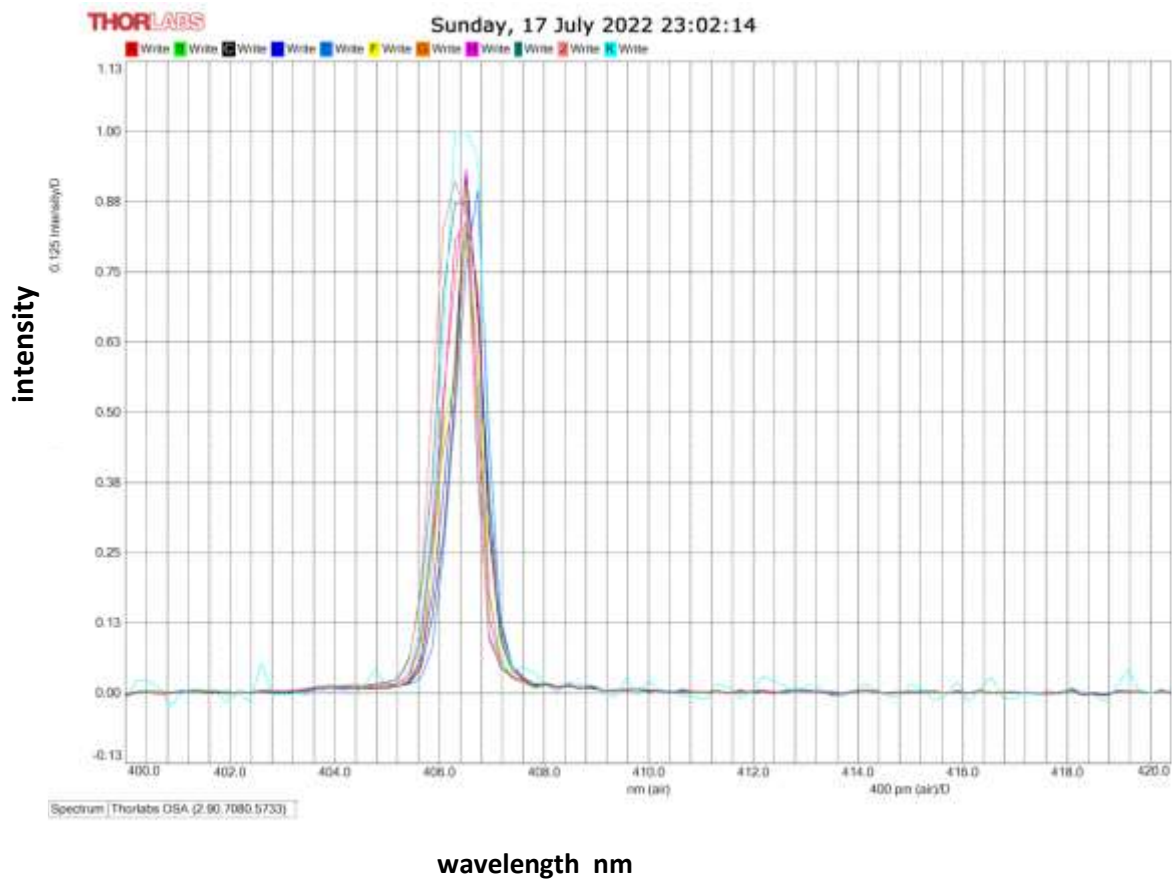


Sample 1.... Sample 2.... Sample 3.... Sample 4....sample 5.... Sample 6....sample 7....  
sample 8....sample 9...sample10....sample(source)

Fig. 4: show intensity peak in pathogenic E.coli

**Table 3:** (E.coli normal flora): Show results of sample, intensity, Peak wavelength nm (air), FWHM(pm)air.

Sample no	Intensity	Peak wavelength nm (air)	FWHM (pm)air
source	1.000000	406.0802002	820.1606058
1	0.8381	406.5158	882.4570
2	0.8229	406.5158	791.3645
3	0.9287	406.5158	634.3673
4	0.9134	406.5158	684.9534
5	0.8962	406.7337	706.9323
6	0.9063	406.5158	739.3869
7	0.8386	406.5158	767.2167
8	0.9340	406.5158	717.5493
9	0.8728	406.5158	812.7075
10	0.9125	406.2980	886.8341



sample 1.... Sample 2.... Sample 3.... Sample4.... Sample 5.... Sample 6....sample7  
 sample 8....sample 9.... Sample 10.... Sample(source)

**Fig. 5:** show laser intensity peak(410nm) in Normal flora *E.coli*

## Conclusion:

The use of optical biosensor multimode – no core - multimode fibre with a 410nm laser source to sensing and differentiate between normal and pathogenic bacteria of E.coli . Through the study, we found that laser intensity (410nm) in state the normal flora bacteria higher than intensity laser (410nm) in state the pathogenic bacteria because the pathogenic bacteria contain many virulence factors(higher absorption). The biosensor is more accurate, quick to diagnose and less expensive.

## References

- Alageedi, Shahad K., and Layla M. Alameri. 2019. "Assessment of variation in luteinizing hormone (LH) level among females by using single mode fiber optical biosensor (SMF)." *Biochem. Cell. Arch.* Vol. 19, No. 2, Pp. 4221-4224, 2019.
- Alameri, L. M., Mansour, T. S., Rashid, F. F., & Belal, S. J. (2020). Design in line lma-10 photonic crystal fiber mzi for detection and investigation of beta thalassemia. *Medico-Legal Updat.*, 20(1), 591-595.
- Best L, Prasse D, Bathia J, Rühlemann MC, Boersch K, Jaspers C, Sommer F. Functions of the Microbiota for the Physiology of Animal Meta organisms. *J Innate Immun.* 2019;11(5):393-404. Available:<https://doi.org/10.1159/000495115>
- Clermont, O., Bonacorsi, S., and Bingen, E. (2000). Rapid and simple determination of the Escherichia coli phylogenetic group. *Appl. Environ. Microbiol.* 66, 4555–4558. doi: 10.1128/AEM.66.10.4555-4558.2000
- Dekaboruah, Elakshi, Mangesh Vasant Suryavanshi, Dixita Chettri, and Anil Kumar Verma. 2020. "Human Microbiome: An Academic Update on Human Body Site Specific Surveillance and Its Possible Role." *Archives of Microbiology* 202(8):2147–67.
- Hossain, S. Z., & Mansour, N. (2019). Biosensors for on-line water quality monitoring—a review. *Arab Journal of Basic and Applied Sciences*, 26(1), 502-518.
- Journal, Baghdad Science. 2014. "Inhibition Activity of Saccharomyces Boulardii and Lactobacillus Acidophilus against Pathogenic E.Coli Isolates from Recurrent Urinary Tract Infection in Women In Vitro: Nada S. Rezuqi|Farah Q. Younis." *Baghdad Science Journal* 11(1 SE-article):22–32. doi: 10.21123/bsj.2014.11.1.22-32.
- Kareem, A. U., & Mansour, T. S. (2022). Temporal Pulse Compression Using Double Cladding Polarization Maintaining Fiber Nested Mach-Zehnder Interferometer. 23.
- Lloyd-Price, Jason, Galeb Abu-Ali, and Curtis Huttenhower. 2016. "The Healthy Human Microbiome." *Genome Medicine* 8(1):1–11. doi: 10.1186/s13073-016-0307-y
- Pandey, C. M., & Malhotra, B. D. (2019). 2. Biorecognition Elements in a Biosensor. In *Biosensors* (pp. 19-36). De Gruyter.
- Peltomaa, R., Glahn-Martínez, B., Benito-Peña, E., & Moreno-Bondi, M. C. (2018). Optical biosensors for label-free detection of small molecules. *Sensors*, 18(12), 4126
- Salam, Hadeel, and Mohammed Alabd. 2019. "Assessment of ALT and AST Enzymes Via Optical Sensing A Thesis Submitted to the Institute of Laser for Postgraduate Studies, University of Baghdad in Partial Fulfilment of the Requirements for the Degree of Master of Science in Laser / Biology By Hadeel S." University of Baghdad.
- Saleh, Hiba Taqi. 2020. "Study the Effect of ZnO, Ag Nanoparticles on Bacteria

- with and without 410 Nm Diode Laser.” University of Baghdad Institute
- Shatti, Rawia, and Layla M. H. Al-ameri. 2021. “Optically Sensing for Thyroid Profile Hormones in Blood.” *Medico-Legal Update* 21(2).
- Tenaillon, O., Skurnik, D., Picard, B., and Denamur, E. (2010). The population genetics of commensal *Escherichia coli*. *Nat. Rev. Microbiol.* 8, 207–217. doi: 10.1038/nrmicro2298
- Tallon, P., Magajna, B., Lofranco, C., and Leung, K. T. (2005). Microbial indicators of faecal contamination in water: a current perspective. *Water Air Soil Poll.* 166, 139–166. doi: 10.1007/s11270-005-7905-4
- Wang, Baohong, Mingfei Yao, Longxian Lv, Zongxin Ling, and Lanjuan Li. 2017. “The Human Microbiota in Health and Disease.” *Engineering* 3(1):71–82.
- Whitman, R. L., Nevers, M. B., and Byappanahalli, N. (2006). Examination of watershed-wide distribution of *Escherichia coli* along Southern Lake Michigan: and integrated approach. *Appl. Environ. Microbiol.* 72, 7301–7310. doi: 10.1128/AEM.00454-06
- Yoo, Seung Min, and Sang Yup Lee. 2016. “Optical Biosensors for the Detection of Pathogenic Microorganisms.” *Trends in Biotechnology* 34(1):7–25. doi: 10.1016/j.tibtech.2015.09.012

## الاستشعار والتفريق بين البكتريا الطبيعية والممرضة للاشريكية القولونية باستخدام ليزر ديود 410 نانومتر

ثائر فرحان عكاب الخزاعي ليلي محمد حسن العامري

معهد الليزر للدراسات العليا ، جامعة بغداد ، العراق

### الخلاصة

توفر المستشعرات الحيوية الضوئية خصائص وطرقاً ممتازة للكشف عن البكتيريا عند مقارنتها بتقنيات التحليل التقليدية. يسمح بالكشف المباشر عن العديد من المواد البيولوجية والكيميائية. توجد البكتيريا في جسم الإنسان بشكل طبيعي غير مسببة للأمراض و انواع اخرى مسببة للأمراض ، كما توجد في الكائنات الحية الأخرى. واحدة من هذه البكتيريا هي *Escherichia coli* (E. coli) والتي توجد في جسم الإنسان بشكلها الطبيعي والممرض. تسبب بكتيريا الإشريكية القولونية العديد من الأمراض ، بما في ذلك أمراض المعدة والأمعاء والتهابات الجهاز البولي وغيرها. الهدف من هذه الدراسة هو الاستشعار والتفريق بين بكتيريا الإشريكية القولونية الطبيعية والممرضة. المواد والطرق: المستشعر الحيوي البصري المصنوع من ألياف بصرية متعددة الأوضاع - بدون نواة - متعددة الأوضاع تتميز بين البكتيريا المسببة للأمراض وغير المسببة للأمراض للإشريكية القولونية عن طريق قياس التغير في الشدة لطول موجة الليزر باستخدام مصدر ضوء ليزر 410 نانومتر. ألياف بصرية متعددة الأوضاع - لا نواة - متعددة الأوضاع (MM-NOC-MM) متصلة بمحلل OSA (HR2000) عن طريق محول وأخيراً متصلة بجهاز كمبيوتر لإظهار النتيجة. النتائج: شدة الضوء المرسل المسجل في حالة البكتيريا المسببة للأمراض أقل من شدة الضوء المرسل المسجل في حالة البكتيريا غير الممرضة. الخلاصة: تم الحصول على هذه النتائج بسبب الاختيار الأمثل والأفضل لطول موجة الليزر المستخدم مع بكتيريا الإشريكية القولونية.



## Effectiveness of 980nm diode Laser in reduction the diameters of exposed dentinal tubules for hypersensitive tooth

Rana H. Haider<sup>1</sup>, Mohammed K. Dhahir<sup>1</sup>, Salah A. AlKurtas<sup>2</sup>

\*Corresponding Authors: Rana.alshamary00@gmail.com

mohammed@ilps.uobaghdad.edu.iq

Sa\_alkurtas2006@yahoo.com

1. Institute of Laser for Postgraduate Studies, University of Baghdad, Baghdad, Iraq

2. Consultant maxillofacial surgeon, Alkarkh-Hospital, Baghdad, Iraq

(Received 12/11/2022; accepted 14/01/2023)

### Abstracts:

**Background:** The oral cavity is a complex environment, both structurally and functionally, the hard and soft tissues are in close a proximity. Oral tissues subjected to wear throughout the life, that threatened the vitality of the pulp or increase the sensitivity of dentinal tubules. One of the common dental problems is loss of enamel or cementum, which stimulate the nerve ending in or near the pulp and manifested as pain sensation. **Aim of the study:** This study had done to evaluate the effects of 980nm diode Laser in diameters reduction of exposed dentinal tubules analyze the results and morphological changes of irradiated dentine surface by FE-SEM (field emission scanning electron microscope) analysis. **Material and Method:** Thirty-nine human extracted impacted 3<sup>rd</sup> molar teeth were tested in this study and divided into control Group (N=15), pilot study (N=9) and study group (N=15). The study group irradiated with 980nm diode Laser to the occlusal surface of the teeth after the application of 17% EDTA (Ethelyn diamine tetra acetic acid) for smear layer removal. The intra-pulpal temperature recorded for every second and monitored for 120s from the first second of irradiation by a thermometer (prosket MT-1820, 1st Edition, 2016, Taiwan), for detection the recovery time of initial tooth temperature. FE-SEM analysis to all teeth (control, pilot and study groups) for assessment the morphological changes after surface irradiation. **Results:** FE-SEM analysis to the irradiated surface show significant reduction in diameters of the exposed dentinal tubules irradiated by 980nm diode Laser. **Conclusion:** The selected parameters (1.5W/10s, 276.3W/cm<sup>2</sup>) were able to seal exposed dentinal tubules without any sign of cracks or fissures. **Suggestion:** The parameters used with this study (1.5W, 10s, 276.3W/cm<sup>2</sup>) can be utilize in the future treatment protocol to the management of dentinal hypersensitivity.

**Key words:** Dentine hypersensitivity; etiological factors; Dental pain; Diode Laser; scanning electron microscope.

## **Introduction:**

Dentine hypersensitivity (DH) is a most frequently encountered dentist in daily work and most widespread oral pathological problem (Amino shariae et al, 2021). Any procedure, that cause a change in the architecture of the protective enamel and dentine layers, may lead to pulpal inflammation and increased thermal sensitivity, Besides the procedures that increases dentine permeability through the alterations to the integrity of the enamel and dentine such as; decay, trauma, and tooth wear can give rise to symptoms of dentinal hypersensitivity (Ansari et al, 2013). DH is characterized by localized, short, sharp pain in exposed dentine in response to external thermal, mechanical, chemical, or osmotic stimuli, which cannot be attributed to any other form of dental defect or pathology, it may be associated with a number of factors including erosion, abrasion, attrition and may be associated with periodontal treatments or surgery (Bamise et al, 2011). DH manifested by an exaggerated response of exposed dentine to a nonharmful stimuli (mechanical, thermal, tactile, chemical or osmotic), that usually cause no response in a healthy tooth (Boreges et al, 2012). According to the hydrodynamic theory, as believed by [Brannström & Astrom [1963], the fluid movement in response to external stimuli can stimulate the pulpal afferent (A $\delta$ ) fibers in or near the pulp that produce pain sensation (Bordin et al, 2019). The velocity of fluids movement in dentinal tubules depends on the nature of stimuli, in thermal stimuli the cold applications cause contraction of fluids, that evoke rapid movement of fluids than hot stimuli, while hot stimuli cause expansion of fluids. So, the cold stimuli cause more painful sensation than hot one (Bubteina et al, 2015). The prevalence rate of dentinal hypersensitivity ranging (8-74%) among population, the appearance of the disease and prevalence distribution differs due to the differences in dietaries, populations and habits being more frequent in patients aged between 30 and 40 years (Borges et al, 2012). The treatment strategies of dentinal hypersensitivity either self-applied (in-home) or proficient-applied (in-office) depends on two ways; nerves blocking and/block the dentinal tubules to reduce the

fluids movements in exposed dentine (Bamise et al, 2011). The conventional desensitizing agents with variables form (varnish, gels, or restorative materials) have a limit potential effect on dentinal hypersensitivity, that need frequent sessions or re-applied after a period of time (Chetan et al, 2022). Different laser types have been tested for dentinal hypersensitivity treatment. Laser can be applied in two levels, high level Laser therapy (HLLT) with energy density more than (4 J/cm<sup>2</sup>) and Low level laser therapy (LLLT), so the optical effects on biological tissues differs accordingly (Cristina et al 2017). The HLLT occludes dentinal tubules by melting and re-solidifying effects. While, the LLLT have photo-biomodulation (PBM) effects on biological tissues (Cronshaw et al, 2022). PBM effects in dentine sensitivity are; analgesic effect and an increase in cellular metabolic activity of the odontoblasts. Thus, enhance the production of tertiary dentine or reparative dentine. So, reduce the symptoms of hypersensitivity. The bio-modulatory effects of LLLT through minimize pain sensation, and reduce inflammatory processes (Femiano et al, 2020). The applications of lasers can be used mainly in two forms, by means of direct and indirect method, respectively. The direct method involves only the use of lasers and indirect method involves application of certain chemical agents (NaF or SnF<sub>2</sub>) and then irradiating the area with the lasers (Chetan P. Raut et al, 2022). The combined laser treatment and fluoridation result in permanent integration of fluoride in the dentinal tubules that give immediate and prolong results, due to synergistic effects of Fluoride with Laser (Femiano et al, 2013). This research study was carried in an attempt to select more suitable parameters with 980nm diode Laser, that give powerful reduction in diameters of exposed dentinal tubules with tooth temperature elevation below the breakdown tolerance of the pulp (5.5<sup>0C</sup>).

## **Material and Method;**

### **1. Sample collection and preparation:**

Thirty-nine Human, extracted, impacted 3<sup>rd</sup> teeth were used in this study. Any fractured, carious or cracked teeth were excluded. The

outer surface of the teeth cleaned from debris and remnant cementum with ultrasonic scaler and then the teeth had immersed in thymol solution (0.1%) for 24 hours to prevent bacterial growth and perceived the lubrication of the samples. The teeth were suctioned transversely (1mm) apical to cements enamel junction with a double-faced diamond bur (22mm) under water cooling with contra-angled handpiece at low speed (300 rpm), the contra-angled handpiece fixed to Surveyor holding by a clamp and the tooth fixed to the tooth holder (Prosket PD-376, Taiwan) for cutting, then one canal prepared with SX-file V-Taper, irrigated with distilled water and then dried with paper points, the probe of thermocouple inserted in prepared canal opposite to the irradiated surface and the other end of thermocouple was fixed to the apical orifice of the root with light cure composite resin for proper sealing from the outer environments. The suctioned surface of teeth polished with non-Fluoride paste for (30s) and dried with air blast for (30s), then the surface coated with 17% EDTA (Ethylene diamine tetra acidic acid) for (three min.) according to manufactured of smear layer removal, then the teeth immersed in ultrasonic cleaner for (two min.) and dried with air blast for (30s), then the samples are ready for irradiation with (980nm) diode Laser. The teeth are fixed in water path with temperature fixed at 37°C to approximate the temperature of the oral cavity, the other end of thermocouple connected to the thermometer for monitoring the tooth temperature while irradiated the dentine surface. The initial temperature recorded, that represents the pulp roof temperature is ( $\tau_1$ ) and the maximum temperature recorded at the exposure time is ( $\tau_2$ ), the change in tooth temperature during irradiation is calculated by ( $\Delta\tau = \tau_2 - \tau_1$ ). Pulp chamber temperature monitored for 120s from the first second of irradiation time to record the time of temperature recovery of the tooth.

### **2. Irradiation and temperature measurement for the study group:**

This study done on 15 teeth for the study Group (G1), the root of the teeth immersed in water path with the probe of thermocouple in position, the teeth fixed with a stainless- steel

rack, the handpiece of diode Laser fixed with a clamp 1mm from the irradiated dentine surface. According to the previous two pilot studies the selected parameters were (1.5W/10s), that are used in this study, the power density was ( $276.3\text{W}/\text{cm}^2$ ), that had determined by measuring the spot size which was ( $542723.690\mu\text{m}^2$ ), then after 40s when the pulp roof temperature reaches the steady state in water path, the teeth irradiated with 980nm diode Laser and the temperature recorded every second for 120s, which was (10s) exposure time and (110s) observation time, for recording the maximum temperature elevation within exposure time and the recovery time for the irradiated tooth within observation period.

### **3. SEM measurement:**

An SEM study was conducted to evaluate the extent to which the applied treatment method blocked the exposed dentinal tubules. All the teeth in this study (control, pilot and study group) analyzed with FE-SEM from (Inspect<sup>TM</sup> F50, FEI, Europe) to evaluate the morphological changes to the irradiated dentine surface. First, the specimens were numbered and attached to the single target plasma coater under pressure 18 Pa, 11mA for 20s, then the samples were placed in FE-SEM device for evaluation the morphologic changes in dentine surface with comparison to the morphology of control group and under magnification taken to each sample at (2500X, 5000X and 10000X).

**Results:** In the present study, the diameters of exposed dentinal tubules assessed for control and the irradiated dentine surface for G1, with FE-SEM analysis as show in figure (1) in page (4). Statistical analysis was performed using the SPSS (v 20, France) for Windows. Post hoc test shows significant reduction ( $P \text{ value} \leq 0.05$ ) in diameter for study group (G1) after irradiation with (1.5W, 10s,  $273.6\text{W}/\text{cm}^2$ ) 980nm diode Laser, the mean value of diameters for G1 was ( $0.66\mu\text{m}$ ), while for control group was ( $1.79\mu\text{m}$ ).

There was very high significant difference between control group and G1 regarding the



Test of Normality done by Kolmogorov-Smirnov<sup>a</sup> and Shapiro-Wilk tests for the exposure time (10s) and the observation time (110s) for G1, which were normally distributed data. Descriptive statistics for observation time (110s) was done and Post hoc test for comparison between tested

mean. There was significant tooth temperature elevation in time duration (11-20s) within the observation time and gradual reduction in temperature mean values as in table (2).

Table (2): post hoc test for observation time (110s)

G1:980nm Diode Laser	DESCRIPTIVE STATISTICS G1												*P value	
	Exposure time	Observation time												
	G1 S1-S10	G1 S11-20	G1 S21-30	G1 S31-40	G1 S41-50	G1 S51-60	G1 S61-70	G1 S71-80	G1 S81-90	G1 S91-100	G1 S101-110	G1 S111-120		
N	150	150	150	150	150	150	150	150	150	150	150	150	150	<b>0.01</b>
Mean	37.65	<b>A</b> 38.05	<b>B</b> 37.78	<b>C</b> 37.51	<b>D</b> 37.24	<b>D</b> 37.13	<b>D</b> 37.05	<b>E</b> 36.94	<b>E</b> 36.89	<b>E</b> 36.89	<b>E</b> 36.89	<b>E</b> 36.89	<b>E</b> 36.89	
Std. Error of Mean	0.04	0.02	0.02	0.01	0.00	0.00	0.01	0.01	0.01	0.01	0.01	0.01	0.01	
Median	37.76	38.11	37.83	37.46	37.23	37.13	37.10	37.00	36.99	37.00	37.00	37.00	37.00	
Std. Deviation	0.48	0.24	0.20	0.14	0.04	0.04	0.07	0.12	0.12	0.12	0.12	0.12	0.12	
Minimum	36.47	37.52	<b>37.43</b>	37.31	37.15	37.04	36.83	36.69	36.69	36.70	36.70	36.70	36.70	
Maximum	38.36	38.37	38.07	37.77	37.33	37.20	37.11	37.08	37.00	37.00	37.00	37.00	37.00	
<p><b>*Calculate the significant value of the observation time only, the exposure time not involved //Post hoc test was used to calculate the significant differences between tested mean, the letters (A, B, C, D, and E) represented the levels of significant, highly significant start from the letter (A) and decreasing with the last one. Similar letters mean there are no significant differences between tested mean.</b></p>														

Dunnnett test was done for the exposure time (10s) in comparisons of the tested mean with the initial tooth temperature, there were significant differences in tooth temperature mean values from the initial temperature mean values.

Table (3) shows the differences in page (6), and post hoc test for (10s) was done to determine the significant time in which maximum tooth temperature reaches within exposure time, which were in (S8, S9 AND S10) as in table (4) in page (6).

Table (3): Dunnett test (2 sided) for multiple comparisons depended variables: Temp.

(I) GROUPS	(J) GROUPS	Mean Difference (I-J)	Std. Error	Sig.	95% Confidence Interval	
					Lower Bound	Upper Bound
G1S2	G1S1 INITIAL TIME	.31790*	.05938	.000	.1563	.4795
G1S3	G1S1 INITIAL TIME	.58426*	.05938	.000	.4227	.7458
G1S4	G1S1 INITIAL TIME	.80413*	.05938	.000	.6425	.9657
G1S5	G1S1 INITIAL TIME	.98229*	.05938	.000	.8207	1.1439
G1S6	G1S1 INITIAL TIME	1.12329*	.05938	.000	.9617	1.2849
G1S7	G1S1 INITIAL TIME	1.23145*	.05938	.000	1.0699	1.3930
G1S8	G1S1 INITIAL TIME	1.31082*	.05938	.000	1.1492	1.4724
G1S9	G1S1 INITIAL TIME	1.36524*	.05938	.000	1.2037	1.5268
G1S10	G1S1 INITIAL TIME	1.39828*	.05938	.000	1.2367	1.5599

G1:980 nm without Graphite paste// \*The mean difference s significant at the 0.05 level.

Dunnett t-tests treat one group (INITIAL TIME) as a control, and compare all other groups against it.

Table (4): Post hoc test between tested mean for exposure time (10s)

G1:980 nm without Graphite paste	G1S1	G1S2	G1S3	G1S4	G1S5	G1S6	G1S7	G1S8	G1S9	G1S10	P value
Mean	E 36.74	D 37.06	C 37.33	C 37.55	B 37.72	B 37.87	B 37.97	A 38.05	A 38.11	A 38.11	0.001
Std. Error of Mean	0.04	0.04	0.04	0.04	0.04	0.04	0.04	0.05	0.05	0.05	
Median	36.81	37.12	37.38	37.58	37.75	37.89	37.99	38.07	38.13	38.16	
Std. Deviation	0.15	0.14	0.14	0.15	0.16	0.16	0.17	0.18	0.18	0.19	
Minimum	36.47	36.78	37.03	37.24	37.40	37.54	37.64	37.71	37.76	37.79	
Maximum	36.92	37.23	37.48	37.71	37.91	38.07	38.19	38.27	38.33	38.36	

Post hoc test was used to calculate the significant differences between tested mean, the letters (A, B, C, D, and E) represented the levels of significant, highly significant start from the letter (A) and decreasing with the last one. Similar letters mean there are no significant differences between tested mean

The mean value of temperature elevation for G1 component of tooth structure (Ying Liu et al within exposure time was (1.37°C) and recovery time was at (88s) as seen in figure (3) and (4).

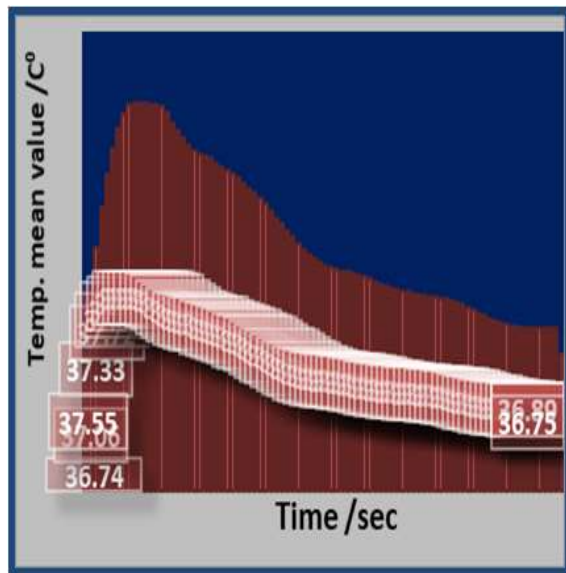
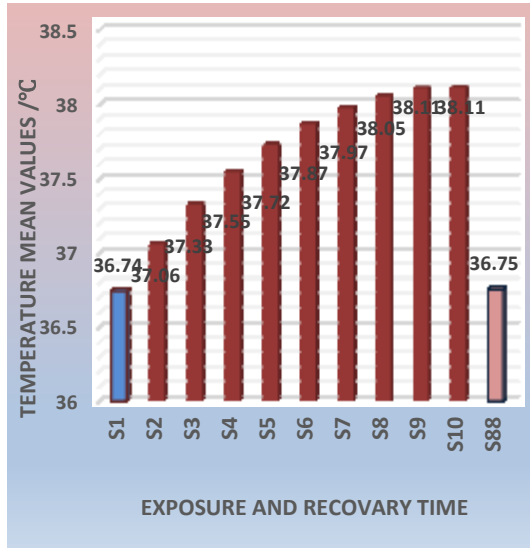


Fig. 4: shows temp. mean value within exposure and recovery time.

**Discussion:**

For dentinal hypersensitivity, many different treatments and techniques have been studied and proposed with identical objectives: to seal dentinal tubules (Hu et al 2019). The prevalence of dentine hypersensitivity is site-specific showed increased predilection in premolars followed by incisors, canines and molars, and more in female than male (Cronshaw et al 2020). Many conventional desensitizing products have been tested to relieve the symptoms of dentine hypersensitivity either by interfering with pulse transmission or by occluding the exposed dentinal tubules to reduce the fluid movements, that have a limitation in time and longevity in treatment of DH, the ideal treatment for DH does not exist, but this is true in case of combination of different protocols (Femiano et al,2020). Laser applications in dentistry come with appositives results in many fields and give a sign in treatment strategies of dentinal hypersensitivity (Hasan Guney Yilmaz et al 2011), many studies have been approved the action mechanisms of diode lasers in dentine hypersensitivity treatments (Mendes et al, 2021). The low output power lasers mediate an analgesic effect related to depressed nerve transmission. Furthermore, it stimulates the dentine forming cell to produce tertiary (Reparative) dentine (Rekha Bilichodmath et al 2018). While, the high-level laser therapy minimize the symptoms of dentine hypersensitivity by modifying the morphology of dentine surface “melting and re-solidification” (Ruaa M. Al-Mafrachi , 2018). In the current study the effects of 980nm diode Laser with the selected parameters (continuous, non-contact mode, 1.5W, 10s, 276.3W/cm2) have a more effective and significant reduction in the diameters of dentinal tubules. The

mechanisms by which the diode Laser occlude exposed dentinal tubules, through the photothermal effects on irradiated dentine surface that results in melting of the organic component of tooth structure (Ying Liu et al 2013). science, the wavelength (800-980nm) diode Laser have poor absorption spectrum in water and hydroxy appetite crystals, so the effects of 980nm diode Laser on dentine surface depending on the absorbing chromophores in dentine surface that absorbed the wavelength 980nm. The main effect of 980nm diode laser is photothermal effect on the collagen fiber (the organic part of dentinal tubules. Furthermore, it has a slight absorption in water, that increase its photothermal effects on dentine surface (*Rajeev Ranjan1* et al 2021). The mean value of temperature elevation was (1.37°C), that below the injury temperature of the pulp (3°C) and the recovery time was at (88s). Previous studies

## References;

Amino shariae, Anita (2021), Current concepts of dentinal hypersensitivity, Journal of Endodontics, Department of Endodontics Case School of Dental Medicine Cleveland State University,47(11): 1696- 1702.

Ansari, Mohammad Ali Erfanzadeh, Mohsen ohajerani, Ezeddin (2013), Mechanisms of laser-tissue interaction: II. Tissue thermal properties, Journal of lasers in medical sciences. 4(3): 99-106.

Bamise, Cornelius Tokunbo Esan, Temitope, Ayodeji, (2011), approaches of dentine hypersensitivity: a literature review, Oral Health, Prev. Dent. 9(4):353-367.

Borges, A Barcellos, D Gomes (2012), Dentin hypersensitivity- etiology, treatment possibilities and other related factors: a literature review, World Journal of Dentistry.3(1): 60-67.

approved that, diode lasers have a multiple role in dentinal hypersensitivity, their occluding effects by making dentine cells degenerate, cause calcium salt deposition, and calcify the closure of dentine tubules (Ruaa M. Al-Mafrachi et al, 2018). Besides, it can stimulate the dentine forming cells (odontoblast) and induces them to produce secondary dentine by the production of secondary reaction (Rekha et al, 2018). Moreover, the analgesic effects through the change in nerve fiber membrane permeability to potassium and sodium (Rajeev Ranjan et al, 2013), increase the peripheral nerve action potentials, and stimulates the formation of neural axon endorphins, which have an analgesic effect (Tabibzadeh et al, 2018). The results of this study a great agreement with that of (Ying Liu et al,2013) and (Umana et al 2013).

Bordin-Aykroyd, Sonia Dias, RB Lynch, (2019), Laser-tissue interaction, EC Dental Science.18(9): 2303-2308.

Bubteina, N Garoushi (2015), Dentine hypersensitivity:a review, J Dentistry. 5(330): 1122-2161.

Chetan Purushottam Raut, Kunal Sunder Sethi, Bhagya shree Kohale,Alefiya (2022), Evaluation of diode laser and stannous fluoride in the treatment of root sensitivity after access flap surgery: Randomized controlled clinical trial, Mamajiwala, Ayush Waran. 37(239): 24-100.

Cristina García-Delaney, Daniel Abad-Sanchez, Josep Arnabat-Domínguez, Eduard Valmaseda-Castellon, Cosme Gay- Escod (2017), Evaluation of the effectiveness of the photo-biomodulation in the treatment of dentin hypersensitivity after basic therapyA randomized clinical trial. J Clin Exp Dent.9(5): e694-702.

Cronshaw, Mark Parker, Steven Anagnostaki, Eugenia Mylona, Valina Lynch, Edward

- Grootveld, Martin (2020), Photobiomodulation dose parameters in dentistry: a systematic review and meta-analysis, *Dentistry Journal*.8(4): 114.
- Femiano, Felice Femiano, Rossella Femiano, Luigi Nucci, Ludovica Minervini, Giuseppe Antonelli, Alessandro Bennardo, Francesco Barone, Selene Scotti, Nicola Sorice, Vittoria (2020), A new combine protocol to treat the dentin hypersensitivity associated with non-cariou cervical lesions: a randomized controlled trial, *Applied Sciences*.11(1): 178.
- Femiano, Felice Femiano, Rosella Lanza, Alessandro Festa, Maria Vincenzo Rullo, Rosario Perillo, Letizia (2013), Efficacy of diode laser in association to sodium fluoride vs Gluma desensitizer on treatment of cervical dentin hypersensitivity *Sciences*. 26(4): 214-219.
- Hasan Guney Yilmaz, Sevcan Kurtulmus-Yilmaz, and Esra Cengiz (2011), Long-Term Effect of Diode Laser Irradiation Compared to Sodium Fluoride Varnish in the Treatment of Dentine Hypersensitivity in Periodontal Maintenance Patients: A Randomized Controlled Clinical Study, *Photomedicine and Laser Surgery*. 29(11): 721-725.
- Hu, Meng-Long Zheng, Gang Han, Jian-Min Yang, Meng Zhang, You-Dong Lin, Hong (2019), Effect of lasers on dentine hypersensitivity: evidence from a meta-analysis, *Journal of Evidence Based Dental Practice*. 19(2): 115-130.
- Mendes, Sara Tereza Camelo Pereira, Camila Santos Oliveira, Jannefer Leite de Santos, Vívian Cristina Silva Goncalves, Brenda Barbosa Mendes, Danilo Cangussu (2021), Treatment of dentin hypersensitivity with laser: systematic review, *BrJP*. 4: 152-160.
- Rajeev Ranjan<sup>1</sup>, Kausar Jaha Yadwad<sup>2</sup>, Sudhir R Patil<sup>2</sup>, S Mahantesha<sup>3</sup>, Aslam ARahman, Varun B Bhatia, Efficacy of 980nm diode laser as an adjunct to Snf2 in the management of dentinal hypersensitivity: A controlled prospective clinical study *Journal of dental laser*.2013; 7(2): 66-71.
- Rekha Bilichodmath, R. Kumar, Shiva Prasad Bilichod math and Ume Sameera, Jou (2018), Diode laser in the treatment of dentinal hypersensitivity: A reliable approach, *Journal of dental science*.12(8):56.
- Ruaa M. Al-Mafrachi Lutfi G. Awazli and Mohammed A. Al-Maliky (2018), The Effect of using 940 nm Diode Laser in Comparison with Endoactivator on Radicular Dentin Permeability and Smear Layer Removal (An in Vitro Study), *Iraqi Journal of Lasers*.17(B): 9-15.
- Rajeev Ranjan<sup>1</sup>, Kausar Jaha Yadwad<sup>2</sup>, Sudhir R Patil<sup>2</sup>, S Mahantesha<sup>3</sup>, Aslam A Rahman<sup>4</sup>, Varun B Bhatia<sup>4</sup>, Efficacy of 980nm diode laser as an adjunct to Snf2 in the management of dentinal hypersensitivity: A controlled, respective clinical study *Journal of dental laser*.2013; 7(2): 66-71.
- Tabibzadeh, Zohreh Fekrazad, Reza Esmaeelnejad, Azadeh Shadkar, Mohammad Mostafa Sadrabad, Zahra Khalili Ghojazadeh, Morteza (2018), Effect of combined application of high-and low-intensity lasers on dentin hypersensitivity: A randomized clinical trial, *Journal of Dental Research, Dental Clinics, Dental Prospects*.12(1): 49.
- Ying Liu, Jie Gao, Yan Gao, Shuaimi XU, Xueling Zhan, Buling Wu (2013), In Vitro Study of Dentin Hypersensitivity Treated By 980-nm Diode Laser, *Journal of Lasers in Medical Sciences*.4(3): 111-119.
- Umana, Monica Heysselaer, Danie Tielemans, Marc Compere, Philippe Zeinoun, Toni Nammour, Samir, (2013) Dentinal tubules sealing by means of diode lasers (810 and 980 nm): a preliminary in vitro study, *Photomedicine laser surgery*

## فعالية ( ٩٨٠ نانومتر ) دايود ليزر على انحسار القطر للاوعية السنية المكشوفة لسن فرط الحساسية العاجية

رنا هاشم حيدر\* ، كريم محمد ظاهر ، صلاح عبد الامير القرطاس

معهد الليزر للدراسات العليا - جامعة بغداد

### الخلاصة :

تتضمن الدراسة تحضير ( ٣٩ سن) من أسنان العقل المقموعة جراحياً وأزالة طبقة الميناء كلياً عن سطح الاطباق، وعندما تتم إزالة المينا يؤدي ذلك إلى أن تكون الأنابيب السنية داخل طبقة العاج مكشوفة مما يؤدي الى زيادة حركة السوائل داخل الأنابيب وتحفيز النهايات العصبية القريبة من لب السن وزيادة الأحساس بالألم. حيث تم تقسيم الاسنان الى ثلاث مجاميع المجموعة الاولى هي المجموعة التجريبية لأختيار معاملات مناسبة للتشعيع بالدايود ليزر واستخدم فيها (٩ أسنان) والمجموعة الثانية هي المجموعة الظابطة واستخدم فيها (١٥ سن) والمجموعة الثالثة هي مجموعة الاختبار المشععة بالدايود ليزر وأستخدم فيها (١٥ سنة).

حيث تم تشعيع العينات بالدايود ليزر ذو الطول الموجي ٩٨٠ نانومتر مع معاملات تم اختيارها بأجراء دراستين تجريبية قبل بدء التشعيع لمجموعة الاختبار وقد استخدم (١,٥ واط) ، (١٠ ثانية) وكثافة طاقة ( ٣,٢٧٦ واط/سم<sup>٢</sup>) تم اختيارها بقياس مساحة نقطة التشعيع. وبعد مرور ( ٤٠ ثانية) عن وضع اسنان مجموعة الاختبار داخل الحمام المائي بدأ تشعيع اسنان مجموعة الاختبار.

أظهر فحص المايكروسكوب الماسح الالكتروني أنسداد واضح في الأنابيب السنية المفتوحة بعد التشعيع لمجموعة الاختبار وأظهر التحليل الأحصائي انحسار كبير بقطر الأنابيب السنية المكشوفة مقارنة مع قطر المجموعة الظابطة ، وكان ارتفاع درجة حرارة السن نتيجة التشعيع ضمن الحدود المسموح بها للحفاظ على حيوية السن أما وقت انتعاش السن فقد سجل بالثانية (٨٨) من الثانية الاولى لبدأ التشعيع.



## The effect of nanoelectrodes number and length on enhancing the THz photomixer performance

*Reiam Al-Mudhafar, Hussein Ali Jawad\**

*Corresponding author: Hussein@ilps.uobaghdad.edu.iq*

*Institute of Laser for Postgraduate Studies, University of Baghdad, Baghdad, Iraq*

(Received 23/01/2023; accepted 30/03/2023)

**Abstract:** Despite the distinct features of the continuous wave (CW) Terahertz (THz) emitter using photomixing technique, it suffers from the relatively low radiation output power. Therefore, one of effective ways to improve the photomixer emitter performance was using nanodimensions electrodes inside the optical active region of the device. Due to the nanodimension sizes and good electrical conductivity of silver nanowires (Ag-NWs), they have been exploited as THz emitter electrodes. The excited surface plasmon polariton waves (SPPs) on the surface of nanowire enhances the incident excitation signal. Therefore, the photomixer based Ag-NW compared to conventional one significantly exhibits higher THz output signal. In this work, the effect of Ag-NWs dimensions and number on the incident optical field is investigated by utilizing the Computer Simulation Technology (CST) Studio Suite. The simulation results show that increasing Ag-NWs length to SPP propagation length ratio plays a significant role on the incident field increment due to its effect on reducing the SPP propagation losses. The increment of Ag-NWs number and length in the nanoelectrodes based photomixer can contribute to increase the electric field in the active region by 1.5 times at the longer excitation wavelength (850 nm). As a result of this increment, the THz output power and the conversion efficiency are expected to be enhanced by a factor of five.

**Keywords:** Plasmonics, Silver nanowire, Terahertz photomixer

### 1. Introduction

The CW-THz emitters using photomixing technique offer many distinctive features in terms of compactness, cost, tunability, and wavelength resolution [1 - 3]. A photomixing technique is based on optical beat signal of two CW laser beams of slightly difference frequencies (which must be in THz frequency region). This signal, which oscillates at the two lasers difference frequency, is used to excite a photoconductive material and then modulates the photocarriers generation [4, 5]. The photocarriers are collected by electrodes

and then translated into THz radiation by an antenna connected to the device [6, 7]. However, the conventional photomixer suffers from its low optical to THz conversion efficiency [6, 8]. Several research works have been attempted to improving the THz output power by enhancing the incident optical intensity inside the photomixer [9 - 13]. The high optical intensity improves the gained photocurrent and thus increases the output radiation. In CW-THz photomixer, Ag-NWs are used as nanodimension electrodes to drive and collect the excited carriers of photoconductive material [14, 15]. Due to small size of these

nanowires, the photomixer devices based on Ag-NWs gain remarkable features [14]. The nanodimensions of these metallic wires give rise to reduce the device capacitance. Furthermore, the electric field of surface SPPs excited on the interface between the Ag-NW and the photoconductive material undergoes notable enhancement. Both factors contribute to improve the photogenerated current inside the mixer active area. Therefore, the photomixer based Ag-NW compared to conventional one significantly exhibits higher obtained photocurrent [15].

In this work, the electric field of SPPs on the surface of Ag-NWs placed on photomixer conductive material (GaAs) is investigated. Therefore, the active region comprises the nanoelectrodes and photoconductive material is simulated by utilizing the CST Studio Suite. From the simulation work, the effect of Ag-NWs dimensions and number on the electric field inside the photomixer can be examined and scrutinized.

## 2. Theory

The photomixer output power  $P_{THz}$  in terms of optical incident intensity is expressed as [16]:

$$P_{THz}(\omega_{THz}) = \frac{1}{2} R_A \cdot (E_{DC}^2 I_o^2) \cdot \frac{\tau_c^2 \mu_e^2}{1 + \omega_{THz}^2 \tau_c^2} \quad (1)$$

where  $R_A$  is the antenna radiation resistance,  $E_{DC}$  is the bias field,  $I_o$  is the beat optical intensity,  $\tau_c$  is carriers lifetime,  $\mu_e$  is carriers mobility,  $\omega_{THz} = \omega_1 - \omega_2$  is the THz frequency of beat signal, and  $\omega_1, \omega_2$  are the frequencies of two incident lasers.

The optical to THz conversion efficiency of the photomixer is [17]

$$\eta = \frac{P_{THz}(\omega_{THz})}{P_1 P_2} \quad (2)$$

where  $P_1$ , and  $P_2$  the optical powers of two incident lasers.

In Ag-NW based photomixer, SPP waves are excited on the surface of the metallic wire by laser light polarized along the wire axis [17, 18]. The incident light is scattered from the wire surface generating SPP modes which propagate towards the end of the wire [17, 19]. The propagating SPPs waves generally reflect at the end face of nanowire of finite length. The reflection of surface plasmon at the end face leads to produce modulation of SPPs field on the surface of nanowire. The spectral

modulation depth  $\Delta I/I_{\min}$  on Ag-NW surface can be determined from [20, 21]:

$$\frac{\Delta I}{I_{\min}} = \frac{4RA}{(1-RA)^2} \quad (3)$$

where  $R$  is the Ag-NW end face reflectivity,  $A$  is the propagation loss which is given by [23]

$$A = e^{-L_{NW}/L_{SPP}} \quad (4)$$

where,  $L_{NW}$  is the length of nanowire,  $L_{SPP}$  is the SPP propagation distance is given by [23, 24]:

$$L_{SPP} = \frac{\lambda}{2\pi} \left( \frac{\epsilon_d + \epsilon_{mr}}{\epsilon_d \epsilon_{mr}} \right)^{3/2} \left( \frac{\epsilon_{mr}^2}{\epsilon_{mi}} \right) \quad (5)$$

where,  $\lambda$  is optical wavelength of incident light,  $\epsilon_d$  is the dielectric constant of dielectric material and  $\epsilon_{mr}, \epsilon_{mi}$  are the real and imaginary parts of the metal dielectric constant, respectively.

## 3. Experiment and Results

By using electromagnetic (EM) software program, we evaluated the near field enhancement in the photomixer after exciting SPPs of Ag-NWs. Simulating the entire nanodimension photomixer (the active region and connected antenna) will take up a great deal of calculation time. For this reason, only the active region is simulated rather than simulating the whole device. Consequently, the active region comprises the nanoelectrodes and photoconductive material is simulated by utilizing CST. The electric field distribution is calculated in the photomixer active region for each value of Ag-NWs number and length. Thereafter, we can scrutinize the electric field in each case and investigate the effect of the Ag-NWs structure parameters on the field variation.

The simulation method is described and clarified in two separate parts. The first part presents the descriptions of the structure parameters, dimensions, materials that used in the simulation. The simulation procedure and methods are then explained in the second part.

**Active region of Ag-NWs based photomixer:** Firstly, the Ag-NWs number in the active region is varied with three values (2, 6, and 10 nanowires). Fig. (1) illustrates three active region structures of Ag-NWs based photomixer of different electrodes numbers. Secondly,  $L_{NW}$  is also changed with four values (3, 3.5, 4, and 4.5  $\mu\text{m}$ ). The structures consist of Ag-NWs nanoelectrodes placed on a photoconductive material (the device substrate). Each structure has the area of 10 x 10  $\mu\text{m}^2$ . The

length of the used nanowires is  $4.5\ \mu\text{m}$ , and the gap between their end faces is  $1\ \mu\text{m}$ . GaAs (12.94 relative permittivity) is used as a substrate. The thicknesses of the electrodes and substrate material are  $0.120\ \mu\text{m}$  and  $1\ \mu\text{m}$ , respectively. The structures of 6 and 10 Ag-NWs have 2.5, 1.5  $\mu\text{m}$  electrodes space, respectively, to obtain an even distribution of nanowires on the substrate surface.

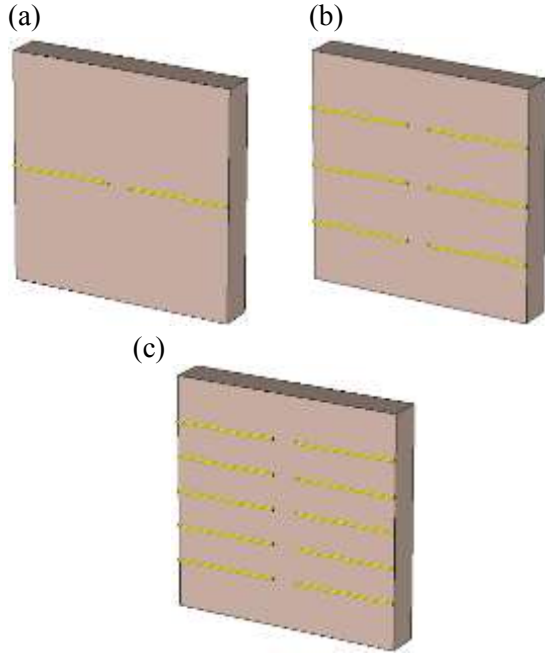


**Fig.1:** Schematic diagram of THz photomixer active regions of different Ag-NWs number: 2, 6, and 10 presented in (a), (b), (c), respectively. The active region of 6 and 10 Ag-NWs have 2.5, 1.5  $\mu\text{m}$  electrodes space, respectively, to obtain an even distribution of nanowires on the substrate surface.

**Simulation of the active region of Ag-NWs based photomixer:** The active region of the photomixer is simulated using CST program to calculate the electric field distribution after illuminating with optical signal. The EM simulation of the electric field distribution on the structure surface is carried out using time domain solver (TDS).

To generate CW-THz radiation, the photomixer active material must be excited by CW optical signal. This optical signal takes a form of beat signal of two optical beams (from two CW semiconductor lasers) which are slightly different in THz frequency range ( $\omega_{THz} = \omega_1 - \omega_2$ ). Since, their frequencies are in optical region and the difference between them is in THz frequency, therefore; their photon energies are close to each other and the photoconductive material interact

with them as an optical beam of single frequency. In the simulation, this beat signal was represented as a plane wave of linear polarization. It is incident on the structure side that contains the nanoelectrodes. The electric field of incident plane wave is 1 V/m. The band gap energy of GaAs is 1.42 eV. Therefore, the laser signal with optical signal near or higher than (1.42 eV) can be used to excite GaAs. The excitation wavelength of conventional photomixer lies in near infrared (NIR) region of EM spectrum (to obtain an optical signal can beat in THz frequency). Therefore, the incident wavelengths 780, 810, and 850 nm are commonly chosen to excite the photomixer.

Because of the inability to work with optical and THz frequency ranges in a single simulation and in order to reduce the large computational time of simulating the nanodimension structures, only the active region is simulated rather than the whole device. 6-mesh-cells per incident wavelength are considered in the structure simulation. On the other hand, a local mesh of 3-cells is set for precisely simulating the electrodes nanodiameter.

In this work, the effect of Ag-NWs electrodes number and length on the optical near field is investigated in the photomixer. At the beginning, the number of Ag-NWs is changed and the consequent variation of the optical electric field in the active region is calculated. In the simulation, the adopted Ag-NWs numbers are: 2, 6, and 10. Thereafter, the Ag-NWs number is fixed and their length is changed with four values: 3, 3.5, 4, and 4.5  $\mu\text{m}$ . Subsequently, the change in the optical electric field is scrutinized for each case.

The simulation results were obtained after illuminating the active region with linearly polarized plane wave of NIR frequency. From the results, we scrutinize the influence of Ag-NWs number and length on the maximum optical near field. At first, the active region structures of three different numbers of Ag-NWs were simulated. The EM simulation using time domain solver is carried out to calculate the resultant electric field on the surface of active region. After the optical illumination, the SPPs wave will be excited on the Ag-NWs surface. The maximum electric field as function of Ag-NWs number for the three incident wavelengths is illustrated in Fig (2). As it can be seen from the figure, the field is significantly enhanced for 780 and 850 nm incident wavelengths when the

nanowires are added to the structure. The electric field is enhanced by the factor of two when the Ag-NW number is changed from 0 to 2 nanowires. The reason behind this enhancement is the plasmonic field induced by Ag-NW. Ag-NW will enhance the field over the whole GaAs surface, therefore; this field is increased with increasing the nanowire number on this surface. A larger number of Ag-NW means more reinforcement to the nanowire plasmonic field on the semiconductor surface.

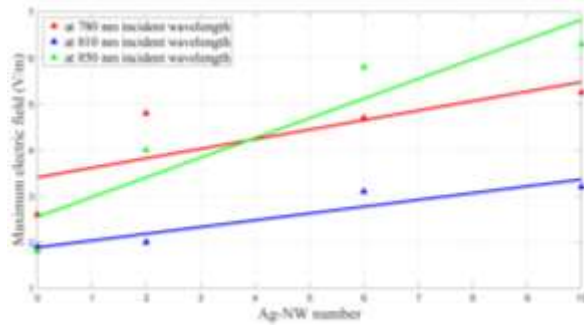


**Fig.2:** Maximum electric field (colored triangles) calculated in the photomixer active region as a function of Ag-NWs numbers. The colored lines represent the results fitted curves.

It can be noticed from Fig. (2) that the plasmonic effect of Ag-NW is small at 810 nm wavelength, since the electric field is not clearly changed after adding Ag-NW. However, this field is significantly increased by a factor of two when the Ag-NW number is changed from 2 to 10. This means that the plasmonic field is small at 810 nm but it exhibits notable increment when the nanowires number is raised due to boosting the light confinement by the Ag-NWs small dimensions. From the results, the maximum electric field is directly proportional to the nanowires number. For larger Ag-NWs numbers, the maximum electric field is noticeable increased on the surface of the active region. The highest increment in the electric field is at 850 nm.

The distribution of the electric field, at 850 nm incident wavelength, in the active regions of different Ag-NWs numbers: 0, 2, 6, 10 are shown in Fig. (3). It can be seen from Fig. (3) that field localizations can be noticed in all structures of Ag-NWs electrodes. It substantially occurs at the two face ends of Ag-NWs. The reason of this noticeable localization is the reflecting of SPPs waves at the end edge of Ag-NW [21].

Figure (4) shows the simulation results of current density in the photomixer active region for different Ag-NWs numbers. The results show that the current density is also directly proportional to the nanowire number. Increasing the electric field with Ag-NW number means higher light intensity can be obtained (more carriers can be generated on the GaAs surface). The large carrier number contributes to enlarge the nanowire conductivity in the active region of photomixer. Therefore, one can see higher value of Ag-NW current density with increasing nanowire number. Due to the small value of the electric field at 810 nm incident wavelength, the current density in the active region is small as compared to that of the other two wavelengths.

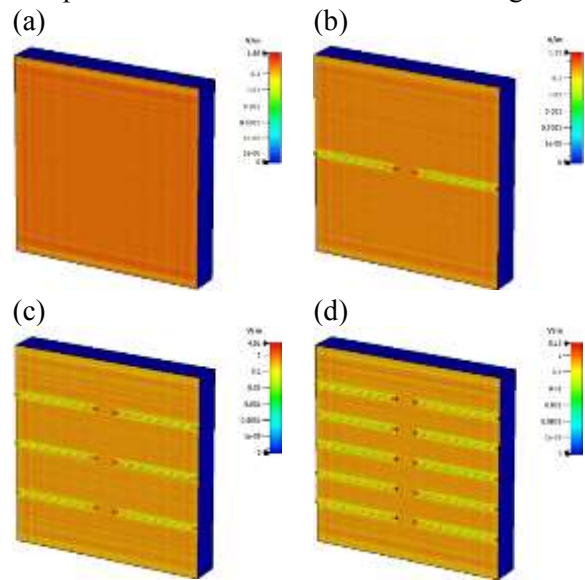


**Fig.3:** Distribution electric field, at 850 nm incident wavelength, in the active regions of different Ag-NWs numbers: 0, 2, 6, 10 presented in (a), (b), (c), and (d), respectively.

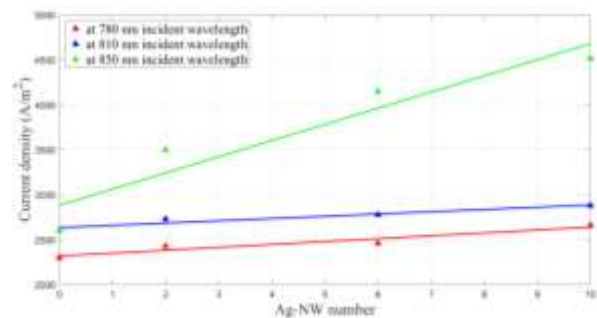


**Fig.4:** Current density (colored triangles) calculated in the photomixer active region as a function of Ag-NWs numbers. The colored lines represent the results fitted curves.

The effect of  $L_{NW}$  on the near electric field is additionally investigated in the photomixer active region. Four active region structures of different Ag-NW lengths ( $L_{NW} = 3, 3.5, 4,$  and  $4.5 \mu\text{m}$ ) were simulated. The active regions have dimensions of  $10 \times 10 \mu\text{m}^2$  and the Ag-NWs is fixed at the number which shows the highest obtained field (10 Ag-NWs). The maximum electric field in the photomixer active region as a function of  $L_{NW}$  is illustrated in Fig. (5). The electric field is increased with  $L_{NW}$ . At 850 nm, the electric field is increased from 4.25 V/m to 6.3 V/m when  $L_{NW}$  is changed from 3  $\mu\text{m}$  to 4.5  $\mu\text{m}$ . The electric field is significantly changed at 810 and 850 nm incident wavelengths. On the other hand, it is less affected by  $L_{NW}$  at 780 nm wavelength. Consequently, the electric field dependency on  $L_{NW}$  is directly proportional to the excitation wavelength, i.e. it is comparatively high at longer wavelength (lower excitation frequency).

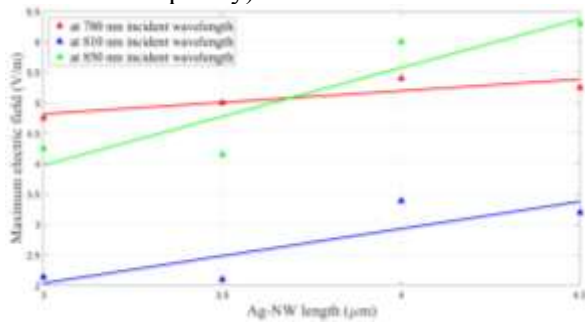


**Fig.5:** Maximum electric field (colored triangles) calculated in the photomixer active region as a function of Ag-NWs lengths. The colored lines represent the results fitted curves.

The electric field distributions in the active regions of four  $L_{NW}$  lengths (3, 3.5, 4, 4.5  $\mu\text{m}$ ) are illustrated in Fig. (6). The calculated current density in the photomixer active region as a function of Ag-NWs number is illustrated in Fig. (7). The current density does not show any change in its values at 780, and 810 nm wavelengths. The small change in electric field with  $L_{NW}$  at 780 nm wavelength causes the relatively stable value of current density at this wavelength. As the electric field is less affected by the Ag-NWs at 810 nm wavelength, the change in current density in the active region is very small at this wavelength.

The propagation losses, which determine the spectral modulation depth  $\Delta I/I_{\min}$  on Ag-NW surface, would have a low value at long  $L_{NW}$  according to Eq. (4). For this reason,

the electric field in the active region shows an increment in its value with  $L_{NW}$ , as shown in Fig. (5). The propagation losses of SPP are calculated by using Eq. (4) for each value of  $L_{NW}$ . Before calculating the propagation losses, we need to determine  $L_{SPP}$  on the Ag-NW interface with GaAs. Eq. (5) is used to calculate  $L_{SPP}$  for all excitation wavelengths. Table (1) shows the calculation results of  $L_{SPP}$  for each wavelength.

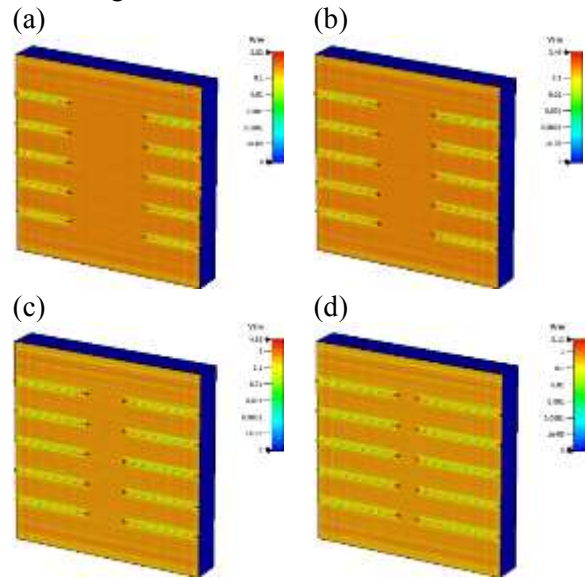


**Fig.6:** Distribution electric field, at 850 nm incident wavelength, in the active regions of different Ag-NWs lengths: 3, 3.5, 4, and 4.5 presented in (a), (b), (c), and (d), respectively.

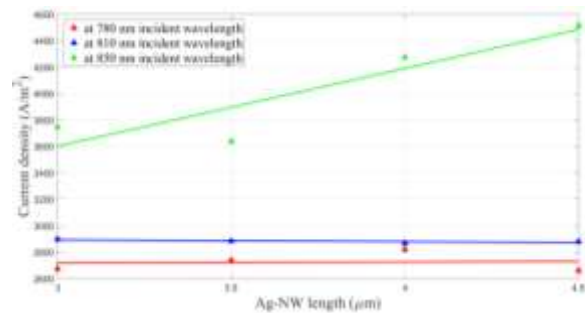


**Fig.7:** Calculated current density (colored triangles) in the photomixer active region as a function of Ag-NWs lengths. The colored lines represent the results fitted curves.

**Table (1)** Calculated SPPs Propagation length on the Ag-NW interface with GaAs substrate for the three excitation wavelengths.

Incident Wavelength (nm)	780	810	850
SPPs Propagation length (μm)	1.7	2.4	3.4

As it can be seen from the table and according to Eq. (5),  $L_{SPP}$  is directly proportional to the excitation wavelengths. By substituting the calculated values of  $L_{SPP}$  in Eq. (4), propagation losses are obtained for each value of  $L_{NW}$ . Fig. (8) shows the calculated propagation losses of SPP on the Ag-NW interface with GaAs as function of  $L_{NW}$  for the three excitation wavelengths. From the results, it can be seen that the propagation losses are decreased at longer  $L_{NW}$ .

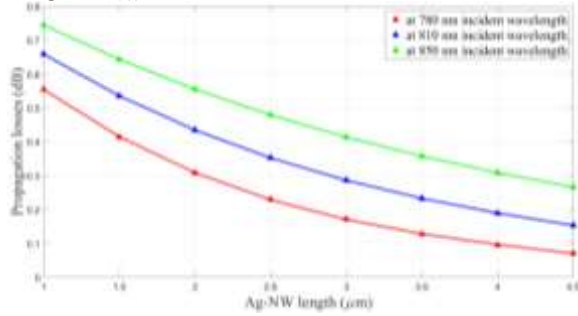


**Fig.8:** Calculated propagation losses of SPP (colored triangles) on the Ag-NW interface with GaAs as function of  $L_{NW}$  for three excitation wavelengths: 780, 810, and 850 nm. The colored lines represent the results fitted curves.

Due to this reduction in the propagation losses of SPP, the electric field in the active region shows an increment in its value with  $L_{NW}$ . Additionally, the longer wavelengths of light show the largest values of propagation losses, as it is seen in Fig. (8). Therefore, the simulation results exhibit remarkable change in the electric field with  $L_{NW}$  at the longer values of wavelengths.

The 780 and 850 nm excitation wavelengths exhibits higher plasmonic effect of Ag-NW, where the electric field is enhanced by the factor of two after adding the nanowires, as shown in Fig. (2). While the field shows a small change in its value at 810 nm wavelength. This change has grown when the Ag-NW number and length are increased. The maximum response of electric field to the change in the Ag-NW number and length is obtained at the two longer wavelengths (810 and 850 nm). This response becomes a small at 780 nm wavelength where the electric field is less affected by Ag-NW number and length, as shown is Fig.(2), and (5) respectively.

The increment of Ag-NWs length and number can contribute to increase the electric field in the active region by 1.5 times at 850 nm. According to Eq. (1), THz output power is quadratically proportional to incident

intensity  $P_{THz}(\omega_{THz}) \propto I_0^2$ . Therefore, it is proportional to the fourth power of the electric field. Since the electric field is increased by 1.5 times with increasing the nanowire parameters, it can be expected from Eq. (1) that  $P_{THz}$  is enhanced by a factor of five. Additionally, the optical to THz conversion efficiency is also improved by a factor of five according to Eq. (2).

Consequently, the length of 4.5  $\mu\text{m}$  is the best  $L_{NW}$  value for THz photomixer emitter that uses two Ag-NWs or more as nanoelectrodes and has a surface area of  $10 \times 10 \mu\text{m}^2$ . Therefore, reducing  $L_{NW}$  in order to decrease Ag-NWs gap and subsequently, minimize the device capacitance leads to bring down the electric field in the active region especially at longer wavelength value.

#### 4. Conclusions

Increasing Ag-NWs length to SPP propagation length ratio plays a significant role on field increment due to its effect on reducing the SPP propagation losses. The increment of Ag-NWs length and number in the Ag-NWs based photomixer can contribute to increase the electric field in the active region by 1.5 times at the longer excitation wavelength (850 nm). The length of 4.5  $\mu\text{m}$  is the best  $L_{NW}$  value for THz photomixer emitter that uses two Ag-NWs or more as nanoelectrodes and has a surface area of  $10 \times 10 \mu\text{m}^2$ . As a result of the notable increment in the electric field, the THz output power and the conversion efficiency are expected to be enhanced by a factor of five.

#### References

- [1] R. Safian, G. Ghazi, and N. Mohammadian, "Review of photomixing continuous-wave terahertz systems and current application trends in terahertz domain", *Optical Engineering*, **58**, 1–28 (2019).
- [2] I. S. Gregory *et al.*, "Optimization of photomixers and antennas for continuous-wave terahertz emission", *IEEE J. Quantum Electron.*, **41**, 717–728 (2005).
- [3] S. Preu, G. H. Döhler, S. Malzer, L. J. Wang, and A. C. Gossard, "Tunable, continuous-wave Terahertz photomixer sources and applications", *J. Appl. Phys.*, **109**, 061301 (2011).

- [4] D. Saeedkia, R. R. Mansour, and S. Safavi-Naeini, "The interaction of laser and photoconductor in a continuous-wave terahertz photomixer", *IEEE J. Quantum Electron.*, **41**, 1188–1196 (2005).
- [5] D. Saeedkia, R. R. Mansour, and S. Safavi-Naeini, "Modeling and Analysis of High-Temperature Superconductor Terahertz Photomixers", *IEEE Trans. Appl. Supercond.*, **15**, 3847–3855 (2005).
- [6] E. R. Brown, "THz Generation by Photomixing in Ultrafast Photoconductors", *International Journal of High Speed Electronics and Systems*, **13**, 497-545 (2003).
- [7] E. Pliński, "Terahertz photomixer", *Bulletin of the Polish Academy of Sciences: Technical Sciences*, **58**, 463-470 (2010).
- [8] S. Lepeshov, A. Gorodetsky, A. Krasnok, E. Rafailov, and P. Belov, "Enhancement of terahertz photoconductive antenna operation by optical nanoantennas: Enhancement of terahertz photoconductive antenna operation by optical nanoantennas", *Laser & Photonics Reviews*, **11**, 1600199 (2017).
- [9] A. D. J. F. Olvera, H. Lu, A. C. Gossard, and S. Preu, "Continuous-wave 1550 nm operated terahertz system using ErAs:In(Al)GaAs photoconductors with 52 dB dynamic range at 1 THz", *Opt. Express*, **25**, 29492 (2017).
- [10] D. J. Ironside, R. Salas, P.-Y. Chen, K. Q. Le, A. Alú, and S. R. Bank, "Enhancing THz generation in photomixers using a metamaterial approach", *Opt. Express*, **27**, 9481 (2019).
- [11] C. W. Berry, N. Wang, M. R. Hashemi, M. Unlu, and M. Jarrahi, "Significant performance enhancement in photoconductive terahertz optoelectronics by incorporating plasmonic contact electrodes", *Nature Communications*, **4**, 1622 (2013).
- [12] S.-H. Yang and M. Jarrahi, "Frequency-tunable continuous-wave terahertz sources based on GaAs plasmonic photomixers", *Appl. Phys. Lett.*, **107**, 131111 (2015).
- [13] R. Al-Mudhafar and H. A. Jawad, "Plasmonic hybrid terahertz photomixer of graphene nanoantenna and nanowires", *IJECE*, **12**, 2711 (2022).
- [14] S. Al-Daffaie, O. Yilmazoglu, F. Kuppens, and H. L. Hartnagel, "1-D and 2-D Nanocontacts for Reliable and Efficient Terahertz Photomixers", *IEEE Trans. THz Sci. Technol.*, **5**, 398–405 (2015).
- [15] A. J. Jumaah, S. Al-Daffaie, O. Yilmazoglu, and T. Kusserow, "Continuous-wave terahertz emitter with hybrid nanoelectrodes based on graphene and nanowire", *OSA Continuum*, **3**, 1826 (2020).
- [16] H. Arenhövel and D. Drechsel, Eds., "*Principles of Terahertz Science and Technology*", Berlin; New York: Springer-Verlag, (1979).
- [17] Z. Ruan, G. Veronis, K. L. Vodopyanov, M. M. Fejer, and S. Fan, "Enhancement of optics-to-THz conversion efficiency by metallic slot waveguides", *Optics express*, **17**, 13502-13515 (2009).
- [18] A. W. Sanders, D. A. Routenberg, B. J. Wiley, Y. Xia, E. R. Dufresne, and M. A. Reed, "Observation of Plasmon Propagation, Redirection, and Fan-Out in Silver Nanowires", *Nano Lett.*, **6**, 1822–1826, (2006).
- [19] P. Venugopalan, Q. Zhang, X. Li, and M. Gu, "Polarization-sensitive characterization of the propagating plasmonic modes in silver nanowire waveguide on a glass substrate with a scanning near-field optical microscope", *Opt. Express*, **21**, 15247, (2013).
- [20] Z. Fang, Y. Lu, L. Fan, C. Lin, and X. Zhu, "Surface Plasmon Polariton Enhancement in Silver Nanowire–Nanoantenna Structure", *Plasmonics*, **5**, 57–62, (2010).
- [21] H. Ditlbacher *et al.*, "Silver Nanowires as Surface Plasmon Resonators", *Phys. Rev. Lett.*, **95**, 257403, (2005).
- [22] T. Laroche and C. Girard, "Near-field optical properties of single plasmonic nanowires", *Appl. Phys. Lett.*, **89**, 233119, (2006).
- [23] D. Buczyńska *et al.*, "Correlating Plasmon Polariton Propagation and Fluorescence Enhancement in Single Silver Nanowires", *J. Phys. Chem. C*, **124**, 15418–15424, (2020).
- [24] M. Jablan, H. Buljan, and M. Soljačić, "Plasmonics in graphene at infrared frequencies", *Phys. Rev. B*, **80**, 245435, (2009).
- [25] A. S. Kalmykov, R. V. Kirtaev, D. V. Negrov, P. N. Melentiev, and V. I. Balykin, "Surface plasmon wave propagation length measurement at a telecom wavelength", *Laser Phys. Lett.*, **17**, 045901, (2020).

## تأثير عدد وحجم الأقطاب النانوية على أداة الدامج الضوئي لاشعة THz

ريام ضياء محمدرضا حسين علي جواد

معهد الليزر للدراسات العليا ، جامعة بغداد ، بغداد ، العراق

**الخلاصة:** بالرغم من السمات المميزة لباعث الموجة المستمرة (CW) تيراهيرتز (THz) باستخدام تقنية المزج الضوئي ، إلا أنه يعاني من طاقة خرج إشعاع منخفضة نسبيًا. لذلك ، كانت إحدى الطرق الفعالة لتحسين أداء باعث المزج الضوئي هي استخدام أقطاب نانوية داخل المنطقة الضوئية النشطة للجهاز. نظرًا للأحجام النانوية والتوصيل الكهربائي الجيد للأسلاك النانوية الفضية (Ag-NWs) ، تم استغلالها كأقطاب باعث THz. تعمل موجات البلازمونات السطحية (SPPs) المثارة على سطح الأسلاك النانوية على تعزيز إشارة الإستثارة الساقطة. لذلك ، فإن المزج الضوئي القائم على-Ag-NW مقارنة بالآخر التقليدي يعرض بشكل ملحوظ إشارة خرج THz أعلى. في هذا العمل ، تم التحقيق في تأثير أبعاد Ag-NWs وعددها على المجال الضوئي الساقط من خلال استخدام برنامج Studio Simulation Technology (CST). أظهرت نتائج المحاكاة أن زيادة طول Ag-NWs إلى نسبة طول انتشار SPP تلعب دورًا مهمًا في زيادة المجال الساقط نظرًا لتأثيرها على تقليل خسائر انتشار SPP. يمكن أن تساهم الزيادة في عدد Ag-NWs وطولها في المزج الضوئي المستند إلى الأقطاب النانوية في زيادة المجال الكهربائي في المنطقة النشطة بمقدار 1.5 مرة عند الطول موجي الأطول (850 نانومتر). نتيجة لهذه الزيادة في المجال الكهربائي ، من المتوقع أن يتم تعزيز قدرة خرج THz وكفاءة التحويل بمعامل خمسة.



## Performance Study of Polarization Beam Splitters Based on Horizontal Slot Waveguide Operating at 700nm Wavelength

Salwa Marwan Salih\*, Shelan Khasro Tawfeeq

Institute of Laser for Postgraduate Studies, University of Baghdad, 10070 Baghdad, Iraq

Corresponding author: [salwa.saleh1001@ilps.uobaghdad.edu.iq](mailto:salwa.saleh1001@ilps.uobaghdad.edu.iq)

(Received 16/04/2023; accepted 25/05/2023)

**Abstract:** Polarization beam splitter (PBS) integrated waveguides are the key components in the receiver of quantum key distribution (QKD) systems. Their function is to analyze the polarization of polarized light and separate the transverse-electric (TE) and transverse-magnetic (TM) polarizations into different waveguides. In this paper, a performance study of polarization beam splitters based on horizontal slot waveguide has been investigated for a wavelength of 700 nm. PBS based on horizontal slot waveguide structure shows a polarization extinction ratio for quasi-TE and quasi-TM modes larger than 15 dB with insertion loss below 1 dB and a bandwidth of ~7 nm. Also, the fabrication tolerance of the structure is analyzed.

**Keywords:** Polarization beam splitter, coupling mode, extinction ratio

### 1. Introduction

Silicon photonics has attracted attention for building high-density photonic integrated circuits due to its compatibility with mature complementary metal-oxide-semiconductor (CMOS) technology [1]. The polarization dependence characteristics can be caused by high index contrast and asymmetric structure, therefore a polarization diversity such as a polarization beam splitter is required [2].

The function of PBS is to separate the transverse-electric (TE) and transverse-magnetic (TM) polarizations of polarized light into different waveguides. The performance of PBS depends on important parameters which are polarization extinction ratio (PER), insertion loss (IL), operating bandwidth, and fabrication tolerance [3].

Different structures of PBSs have been demonstrated such as multimode interferometers

(MMIs) [4], Mach-Zehnder interferometers (MZIs) [5], gratings [6], hybrid plasmonic waveguides [7], directional couplers including symmetric and asymmetric waveguides [8] and slot waveguides [9].

MMI and MZI PBSs induce large insertion loss and footprint, while grating-based structures can achieve a small footprint but with large scattering losses [8],[10]. Using hybrid plasmonic waveguides can shorten the structure length but this type of waveguide suffers from high losses due to metal absorption [11]. PBSs based on symmetric directional couplers are preferred due to their simple design and good performance [12]. While asymmetric directional coupler (ADC) structures require two or more different waveguides to increase the refractive index contrast and attain PBS with a high extinction

ratio, fabrication tolerance, and small footprint [13].

Slot waveguides have been employed recently due to their strong field confinement in the low refractive index nanoscale slot region. A slotted waveguide consists of a layer of low refractive index material sandwiched between two layers of high refractive index materials so that light is mostly confined in the slot region. They can be classified into two categories; horizontally oriented slots within which transverse magnetic (TM) is confined and vertically oriented slots for transverse electric (TE) polarization confinement [14].

Various schemes using slot waveguides have been proposed such as half-etch horizontal slot waveguides [15], PBS assisted by subwavelength grating in triple waveguide directional coupler [16], asymmetric silicon slot-waveguide-assisted [17], and horizontal nanoplasmonic slot waveguides [18].

Recently, integrated photonic technology has been emerged in QKD research, with a series of photonic chips designed for QKD applications [19]. The stability of the QKD system is improved and its cost may be significantly reduced by integrating the optical components of the QKD system, including single-photon sources, that operates in the visible region on a single photonic chip [20],[21].

Free-space QKD generally uses short wavelength due to low atmospheric absorption and efficient operation of Si single photon detector [22]. Thus, different types of PBSs have been developed at visible wavelength [23],[24].

In this paper, we will investigate the operation of PBS based on a dual-channel directional coupler horizontal slot waveguide (DC-HSW) at a wavelength of 700 nm. The integrated PBS in the receiver chip is required to analyze the polarized light sent by single-photon sources for QKD systems based on the BB84 protocol operating at 700 nm. The devices were numerically simulated using COMSOL Multiphysics 6.0 by 2D and 3D frameworks. The device is patterned on silicon on an insulator substrate with air as an upper cladding.

This paper is organized as follows: Section 2 describes the design of the PBS based on dual-channel (DC-HSW), the optical properties, and its wavelength dependence. Section 3 is related to fabrication tolerance for PBS based on dual-channel (DC-HSW). Finally, the conclusions are presented in Section 4.

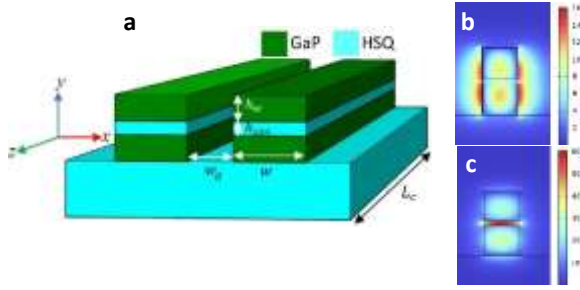
## **2. Design of the PBS based on dual-channel (DC-HSW)**

Figure 1(a) shows the schematic structure of PBS based on dual-channel (DC-HSW). The structure consists of a slot layer of hydrogen silsesquioxane (HSQ) sandwiched between two layers of gallium phosphide (GaP). The refractive indices of air, HSQ, and GaP are (1, 1.41, and 3.2543) respectively. The slot layer supports the optical signal to be guided at a wavelength of 700 nm.

In the 2D framework, the dimensions of a single horizontal slot waveguide (HSW) were found by fixing the slot height,  $h_{slot} = 30$  nm, and tuning the width and height of GaP layers  $w$  and  $h_w$  respectively. The optimal dimensions for  $w$  and  $h_w$  are 130 nm and 200 nm respectively.

Figures 1(b) and 1(c) show the transverse mode profile for quasi-TE and quasi-TM modes for a single HSW. The quasi-TM mode is strongly confined in the slot region due to discontinuity between high and low refractive index regions.

When the light propagates in such a dual-channel DC, the guiding behavior of the total device can be viewed as the summation of waves propagating in even and odd modes with effective indices  $n_e$  and  $n_o$  respectively, as shown in Figures 2(a)-2(d). These modes can be observed due to the differences in the field continuity at boundaries between the core and the cladding. The evolution of the effective index of each corresponding waveguide mode as a function of the waveguide width ( $w_g$ ) is shown in Figure 2 (e).



**Fig. 1:** (a) Schematic of a PBS based on dual-channel (DC-HSW). (b) Transverse field distribution of quasi-TE mode and (c) quasi-TM mode in single HSW

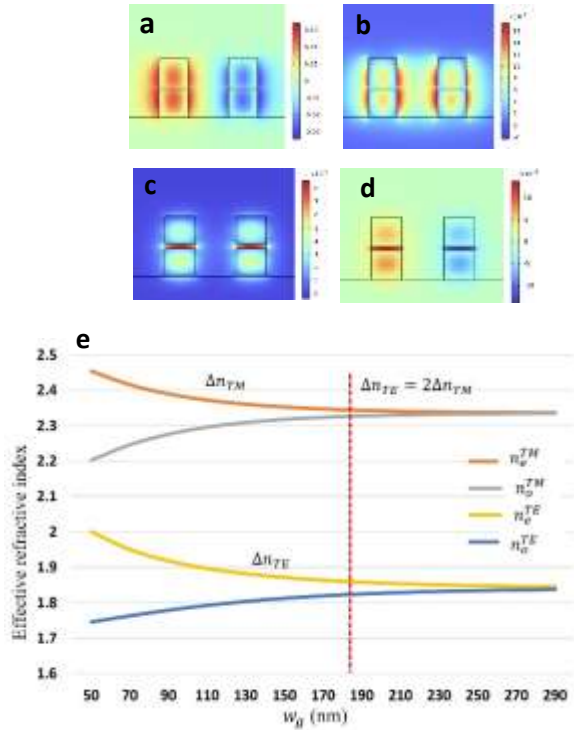


**Fig. 2:** Transverse field distribution of quasi-TE and quasi-TM modes in dual-channel waveguides. (a) even quasi-TE mode (b) odd quasi-TE mode (c) even quasi-TM mode (d) odd quasi-TM mode and (e) the effective indices of even and odd of quasi-TM ( $n_e^{TM}$ ,  $n_o^{TM}$ ) and even and odd of quasi-TE ( $n_e^{TE}$ ,  $n_o^{TE}$ ) as a function of the gap width ( $w_g$ )

As it appears, when  $w_g$  decreases, the effective index difference between even and odd modes ( $\Delta n = |n_e - n_o|$ ) increases because of the coupling between the propagating optical signals in both waveguides. Meanwhile, when  $w_g$  increases, the  $n_e$  and  $n_o$  modes converge to the effective index of individual HSW. In this case,

the dual channels act as independent horizontal slot waveguides.

Following the supermode solution method [25],[26], the coupling length ( $L_c$ ) required to transfer the power completely from the input to adjacent waveguides in a dual-channel DC is related to the difference between the effective indices of  $n_e$  and  $n_o$  for each quasi-TE and quasi-TM mode.

$$L_c = \frac{\pi}{k_0(n_e - n_o)} = \frac{\pi}{k_0\Delta n} \quad (1)$$

Where  $k_0 = \frac{2\pi}{\lambda_0}$  is the propagation constant in free space at the operating wavelength  $\lambda_0$ .

As the width of GaP must satisfy ( $w < 2h_w + h_{slot}$ ), the quasi-TM mode has strong confinement in the slot region while the quasi-TE mode has tails in the waveguide spacing region. As a result, the effective indices of quasi-TE mode may vary significantly as waveguide width increases.

According to the differences mentioned, the ratio of coupling lengths of the quasi-TE mode ( $L_c^{TE}$ ) and quasi-TM mode ( $L_c^{TM}$ ) can be tuned to different values of aspect ratios ( $\frac{w}{h_w}$ ) as a function of the  $w_g$  as shown in Figure (3).

To simplify the design,  $h_{slot}$  was tuned to 30 nm for strong confinement, which will be discussed in section 3. The GaP layers with different aspect ratios, where for each value of  $w = 120, 130, \text{ and } 140$  nm;  $h_w = 180, 190, 200, \text{ and } 210$  nm, were considered to manipulate the birefringence of the horizontal slot structure and the coupling effect based on Equation (1) between the adjacent waveguides.

Based on Figure (3), when  $w_g$  is more than 120 nm, the effective index difference of the quasi-TE mode ( $\Delta n_{TE} = n_e^{TE} - n_o^{TE}$ ) is larger than that of the quasi-TM mode ( $\Delta n_{TM} = n_e^{TM} - n_o^{TM}$ ). By adjusting  $w_g$ , PBS with efficient polarization splitting can be achieved. Based on Equation (1), when  $\Delta n_{TE} = 2\Delta n_{TM}$ , the coupling length ratio is ( $\frac{L_c^{TE}}{L_c^{TM}} = 0.5$ ). The incident light can be efficiently separated into two orthogonally polarized modes propagating in separate output ports. According to Figures (2) and (3), the

optimum dimensions of PBS were tuned using an optimization tool and illustrated in Table 1.

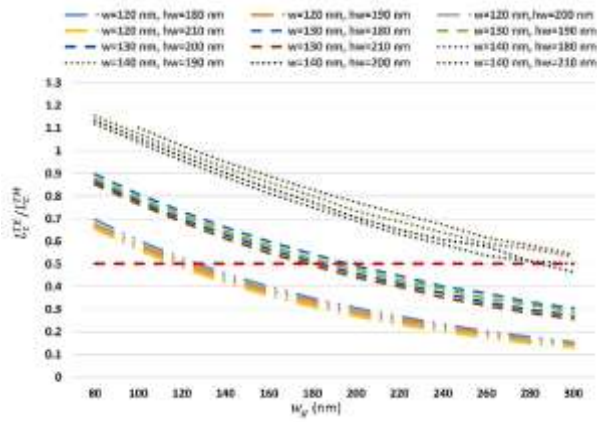


**Fig. 3:** Coupling length ratio of quasi-TE and quasi-TM modes as a function of the gap width ( $w_g$ ) at different aspect ratios ( $\frac{w}{h_w}$ )

The Optimization tool is based on the formula of a general single-objective minimization problem. The goal of the optimization problem is to find the value of the control variables that minimizes (or maximizes) the objective function while considering a number of constraints. One of the optimization methods is the Monte Carlo solver, which samples points randomly within a uniform distribution by a user-specified box. The solver is effective for gathering statistical data for design variations by analyzing the range of values the objective function takes. This method is not stuck in local minima, unlike the other optimization methods implemented in COMSOL Multiphysics. It always analyzes the whole search space specified by the parameter boundaries.

The propagation of light for quasi-TE and quasi-TM modes is shown in Figure (4). It can be observed that quasi-TM mode is completely transferred to the cross port while quasi-TE mode bounced between the adjacent waveguides and is coupled out to the bar port.

**Table (1):** Dimensions of PBS based o dual-channel (DC-HSW)

Substrate width ( $\mu\text{m}$ )	Substrate height ( $\mu\text{m}$ )	$w(\text{nm})$	$h_w(\text{nm})$	$h_{slot}(\text{nm})$	$w_g(\text{nm})$	$L_c(\mu\text{m})$
1.5	1	130	200	30	182	19

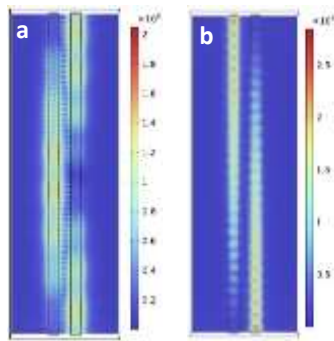


**Fig. 4:** Light propagation for (a) quasi-TE and (b) quasi-TM modes between the adjacent waveguides of PBS based on dual-channel DC-HSW

The wavelength dependence for quasi-TE mode and quasi-TM mode at bar and cross ports of PBS was investigated respectively, as shown in Figure (5). The polarization extinction ratio (PER) and insertion loss (IL) are the keys to the figure of merit for PBS and are defined as:

$$PER_{TE} = 10 \log \frac{P_{bar}^{TE}}{P_{bar}^{TM}} \quad (2)$$

$$PER_{TM} = 10 \log \frac{P_{cross}^{TM}}{P_{cross}^{TE}} \quad (3)$$

$$IL_{TE} = -10 \log \frac{P_{bar}^{TE}}{P_{input}^{TE}} \quad (4)$$

$$IL_{TM} = -10 \log \frac{P_{cross}^{TM}}{P_{input}^{TM}} \quad (5)$$

From Figure (6), it can be noticed that at the operating wavelength of 700 nm PERs are 20.49 dB and 17.36 dB for quasi-TE and quasi-TM modes, respectively. The bandwidths for  $IL < 1$  dB and  $ER > 15$  dB are 6 nm and 7 nm for quasi-TE and quasi-TM modes respectively.

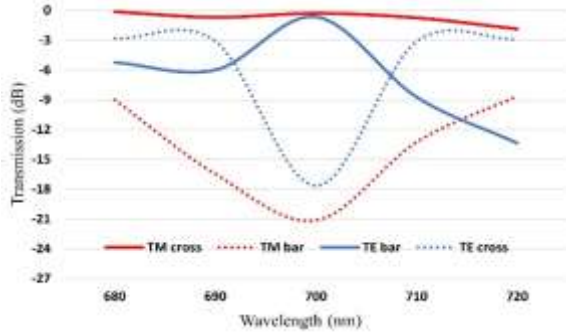


**Fig. 5:** Transmission spectrum for quasi-TE and quasi-TM modes for PBS based on dual-channel DC-HSW

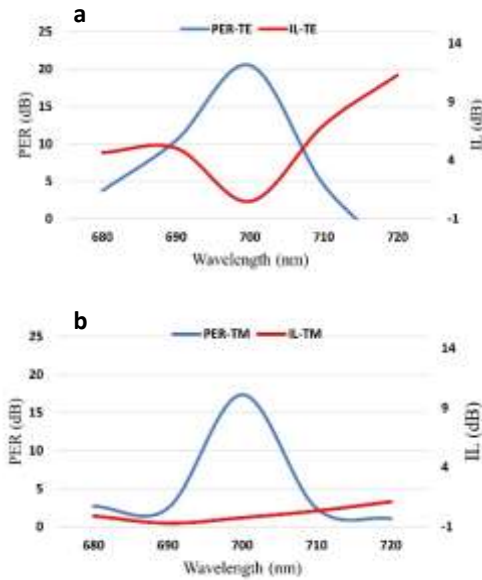


**Fig. 6:** Polarization extinction ratio and insertion loss for (a) quasi-TE and (b) quasi-TM modes for PBS based on dual-channel DC-HSW

The deviation in  $L_c$  shown in Figure (7) was investigated as a parametric study. The deviation is within  $2 \mu\text{m}$  (from 18 to  $20 \mu\text{m}$ ) for keeping the transmission higher than  $-3$  dB. If the deviation range in  $L_c$  is larger than  $2 \mu\text{m}$ , the transmission behavior for quasi-TE mode is varied as the condition in Equation (1) is not fulfilled.

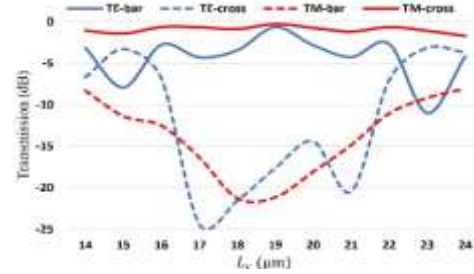


**Fig. 7:** Transmission spectrum of quasi-TE and quasi-TM modes as a function of coupling length ( $L_c$ ) for PBS based on dual-channel DC-HSW

### 3. Fabrication tolerance

A directional coupler based on PBS is usually sensitive to dimension deviation due to fabrication tolerance. Optical lithography and etching are two processes that can be used in the fabrication of PBS based on dual-channel (HSW-DC). These two processes cause deviations in the dimensions of the designed structures.

The fabrication tolerances of  $w$  and  $h_{slot}$  of PBS based on dual-channel (DC-HSW) are shown in Figures 8(a) and 8(b). It can be observed that the tolerance for quasi-TE mode is more critical compared to quasi-TM mode. The deviations in  $w$  and  $h_{slot}$  are limited to a very small range of  $2 \text{ nm}$ . This is because the mode-field distribution and consequently the effective indices for quasi-TE and quasi-TM modes require transverse geometry.

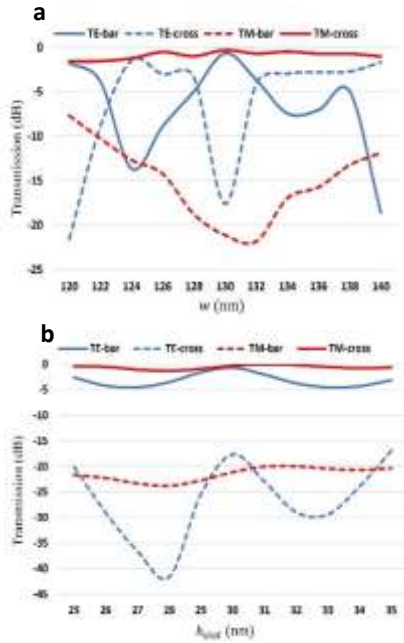


**Fig. 8:** Transmission spectrum of quasi-TE and quasi-TM modes as a function of (a) width of the waveguide ( $w$ ), and (b) slot thickness ( $h_{slot}$ ) for PBS based on dual-channel DC-HSW

Table 2 lists a comparison between the designed structure and other structures mentioned in literature.

#### 4. Conclusion

The performances of PBS based on dual-channel (DC-HSW) has been investigated for a wavelength of 700 nm. With appropriate waveguide dimensions, the structural birefringence in the dual-channel directional coupler formed by HSW on the SOI platform can be precisely controlled. The PER for quasi-TE (TM) mode is 20.49 (17.36) dB respectively with IL < 1 dB and a coupling length of 19  $\mu$ m. It should be noted that the structure's dimensions will vary according to the variation of the wavelength.

#### Acknowledgment

The authors would like to express their gratitude to Dr. Farooq A. Khaleel for his constructive and valuable comments.

**Table (2):** A comparison between the design and other structures mentioned in literature.

References	$\lambda$ (nm)	PER (dB)	IL(dB)	Lc( $\mu$ m)	B.W( nm)	Fabrication tolerance(nm)	Simulation /experimental work
[8]	1550	31.56 (TE) 24.61(TM)	0.4 (TE) 16.2 (TM)	16	> 40	$w = 20$	simulation
[9]	1550	16.8(TE) 14.1(TM)	---	15	C+L bands		Simulation+ experimental
[11]	1550	---	0.55 (TE) 0.92 (TM)	4.05	44	$w_g = \pm 150$	simulation
[14]	1550	25.5 (TE) 23.6 (TM)	<0.2	13.2	100	$w = \pm 10$	simulation
[27]	1550	30 (TE) 40 (TM)	-0.17(TE) -0.22(TM)	11	175	$w_g = \pm 30$ $L_c = \pm 350$	simulation+ experimental
Our work	700	>15 TE and TM	<1	19	7	$w = 2$ $L_c = 2000$	simulation

**References:**

- [1] W. Jiang, X. Sun, and B. M. A. Rahman, "Compact and fabrication-tolerant polarization splitter based on horizontal triple-slot waveguide", *56*, 8 (2017).
- [2] D. Wang, Y. Hu, Y. Zeng, W. Wang, Y. Cai, Z. Tu, W. Yue, Q. Fang, and M. Yu, "Compact polarization beam splitter based on a 3-waveguide directional coupler with broad bandwidth performance", 2019 IEEE 16th International Conference on Group IV Photonics (GFP), (2019).
- [3] C.-C. Huang, "Numerical investigations of an ultra-compact polarization beam splitter based on augmented low index guiding and subwavelength grating structures", *8*, 17338 (2018)
- [4] L. Xu, Y. Wang, A. Kumar, D. Patel, E. El-Fiky, Z. Xing, R. Li, and D. V. Plant, "Polarization Beam Splitter Based on MMI Coupler With SWG Birefringence Engineering on SOP", *IEEE PHOTONICS TECHNOLOGY LETTERS*, **30**, 4 (2018).
- [5] Z. Lin, K. Chen, Q. Huang, S. He, "Ultra Broadband Polarization Beam Splitter Based on Cascaded Mach-Zehnder Interferometers Assisted by Effectively Anisotropic Structures", *IEEE Photonics Journal*, **13**, 1 (2021).
- [6] S. Mao, L. Cheng, C. Zhao, And H. Y. Fu, "Ultra-broadband and ultra-compact polarization beam splitter based on a tapered subwavelength-grating waveguide and slot waveguide", *Optics Express*, **29**, 18 (2021).
- [7] Z. Cheng, J. Wang, Y. Huang, X. Ren, "Realization of a compact broadband polarization beam splitter using the three-waveguide coupler", *IEEE Photonics Technology Letters*, **31**, 22 (2019).
- [8] Y. Liu, L. Chang, Z. Li, L. Liu, H. Guan and Z. Li, "Polarization beam splitter based on a silicon nitride-silica-silicon horizontal slot waveguide", *Optics Letters*, **44**, 6 (2019).
- [9] H. Zhang, Y. Huang, S. Das, C. Li, M. Yu, P. Guo-Qiang Lo, M. Hong, and J. Thong, "Polarization splitter using horizontal slot Waveguide", *OPTICS EXPRESS*, **21**, 3 (2013).
- [10] D. Dai, Z. Wang, J. Peters, J. E. Bowers, "Compact Polarization Beam Splitter Using an Asymmetrical Mach-Zehnder Interferometer Based on Silicon-on-Insulator Waveguides", *IEEE PHOTONICS TECHNOLOGY LETTERS*, **24**, 8 (2012).
- [11] J. Chen, D. Gao, "Ultra-compact beam splitter based on hybrid slot waveguides enhanced by silicon nitride ALIG structure", *Optik*, **220**, 165131 (2020).
- [12] N. Zhao, C. Qiu, Y. He, Y. Zhang, Y. Su, "Broadband Polarization Beam Splitter by Using Cascaded Tapered Bent Directional Couplers", *IEEE photonics journal*, **11**, 4 (2019).
- [13] C. Niu, Z. Liu, X. Li, X. Liu, F. Wan, J. Zheng, "High Extinction Ratio Polarization Beam Splitter Realized by Separately Coupling", *IEEE PHOTONICS TECHNOLOGY LETTERS*, **32**, 18 (2020).
- [14] J. Wang, "Design of a compact polarization beam splitter for silicon-based cross-slot waveguides", *JOURNAL OF MODERN OPTICS*, **67**, 15 (2020).
- [15] E. Kempf, P. R. Romeo, A. Gassenq, A. Taute, P. Chantraine, J. John, A. Belarouci, S. Monfray, F. Boeuf, P. G. Charette And R. Orobitchouk, "SiN half-etch horizontal slot waveguides for integrated photonics: numerical modeling, fabrication, and characterization of passive components", *Optics Express*, **30**, 3 (2022).
- [16] T. Huang, Y. Xie, Y. Wu, Z. Cheng, S. Zeng, and P. S. Ping, "Compact polarization beam splitter assisted by subwavelength grating in triple-waveguide directional coupler", *Applied Optics*, **58**, 9 (2019).
- [17] J. Feng, R. Akimoto, and H. Zeng, "Asymmetric Silicon Slot-Waveguide-Assisted Polarizing Beam Splitter", *IEEE Photonics Technology Letters*, **28**, 12 (2016).
- [18] Y. Huang, S. Zhu, H. Zhang, T.-Y. Liow, and G.-Q. Lo, "CMOS compatible horizontal nanoplasmonic slot waveguides TE-pass polarizer on silicon-on-insulator platform", *OPTICS EXPRESS*, **21**, 10 (2013).

- [19] R. Katsumi, Y. Ota, Alto Osada, T. Yamaguchi, T. Tajiri, M. Kakuda, S. Iwamoto, H. Akiyama, and Y. Arakawa, "Quantum-dot single-photon source on a CMOS silicon photonic chip integrated using transfer printing", *APL Photonics*, **4**, 036105 (2019).
- [20] Farooq Abdulghafoor Khaleel, Shelan Khasro Tawfeeq, On the use of Aluminium as a plasmonic material in polarization rotators based on a hybrid plasmonic waveguide, *Iraqi Journal of Laser Laser*, **20**, 2 (2021).
- [21] L. Kong, Z. Li, Congxiu Li, L. Cao, Z. Xing, J. Cao, Y. Wang, X. Cai, And X. Zhou, "Photonic integrated quantum key distribution receiver for multiple users", *Optics Express*, **28**, 12, (2020).
- [22] J.-S. Choe, B.-S. Choi, H. Ko, and C. J. Youn, "Silica PLC-based Polarization Beam Splitter for 780 nm Free-Space Quantum Key Distribution Applications", *Asia Communications and Photonics Conference*, (2016).
- [23] J. -S. Choe, H. Ko, B. -S. Choi, K. -J. Kim, and C. J. Youn, "Integrated Polarization Beam Splitter Module for Polarization-Encoded Free-Space BB84 QKD", 2018 Optical Fiber Communications Conference and Exposition (OFC), (2018)
- [24] T. Sneh, A. Hattori, M. Notaros, S. Corsetti, and J. Notaros, "Design of Integrated Visible-Light Polarization Rotators and Splitters", *Frontiers in Optics + Laser Science (FiO/LS)*, (2022).
- [25] Y.-F. Ma, M.-J. Sung, and D.-W. Huang, "Controlling the polarization dependence of dual-channel directional couplers formed by silicon-on-insulator slot waveguides", *APPLIED OPTICS*, **49**, 36 (2010).
- [26] N.-C. Cheng, Y.-F. Ma, P.-H. Fu, C.-C. Chin, and D.-W. Huang, "Horizontal slot waveguides for polarization branching control", *APPLIED OPTICS*, **54**, 3 (2015).
- [27] Y. Tian, J. Qiu, C. Liu, S. Tian, Z. Huang, and J. Wu, "Compact polarization beam splitter with a high extinction ratio over S + C + L band", *OPTICS EXPRESS*, **27**, 2 (2019).

## دراسة اداء مقسم استقطاب الشعاع المستند على الفتحة الافقية الذي يعمل ضمن نطاق الطول الموجي المرئي

سلوى مروان صالح، شيلان خسرو توفيق

معهد الليزر للدراسات العليا / جامعة بغداد

تعد موجات المتكاملة لتقسيم حزمة الاستقطاب من المكونات الرئيسية في مستقبل أنظمة توزيع المفتاح الكمي. تتمثل وظيفتها في تحليل استقطاب الضوء وفصل الاستقطاب الكهربائي العرضي (TE) والاستقطاب المغناطيسي العرضي (TM) إلى موجات مختلفة. في هذه المقالة، تم التحقق من أداء مقسم استقطاب الشعاع المستند على الفتحة الأفقية الذي يعمل بالطول الموجي 700 نانومتر. يُظهر مقسم استقطاب الشعاع المستند على الفتحة الأفقية نسبة اخمد للاستقطاب لشبه TE وللاستقطاب لشبه TM أكبر من 15 ديسيبل مع خسارة إدخال أقل من 1 ديسيبل وعرض نطاق يبلغ 7 نانومتر تقريباً. كما تم تحليل نسبة الخطأ في التصنيع للتركيب المصمم.